

Experimental Investigation on the Effects of the Fixed Boundaries in Channelized Dry Granular Flows

L. Sarno¹ · L. Carleo¹ · M. N. Papa¹ · P. Villani^{1,2}

Received: 24 January 2017 / Accepted: 27 August 2017 / Published online: 7 September 2017
© Springer-Verlag GmbH Austria 2017

Abstract The dynamics of granular mixtures, involved in several geophysical phenomena like rock avalanches and debris flows, is far from being completely understood. Several features of their motion, such as non-local and boundary effects, still represent open problems. An extensive experimental study on free-surface channelized granular flows is here presented, where the effects of the fixed boundaries are systematically investigated. The entire experimental data set is obtained by using a homogenous acetal-polymeric granular material and three different basal surfaces, allowing different kinematic boundary conditions. Velocity profiles at both the sidewall and the free surface are obtained by using high-speed cameras and the open-source particle image velocimetry code, PIVlab. Significantly, different sidewall velocity profiles are observed by varying the basal roughness and the flow depth. Owing to sidewall friction and non-local effects, such profiles exhibit a clear rheological stratification for high enough flow depths and they can be well described by recurring to composite functions, variously formed of linear, Bagnold

and exponential scalings. Moreover, it has been discovered that transitions from one velocity profile to another are also possible on the same basal surface by merely varying the flow depth. This shape transition is due partly to the sidewall resistances, the basal boundary condition and, in particular, the occurrence/inhibition of basal grain rolling. In most of the experiments, the normal-to-bed velocity profiles and the velocity measurements at the free surface strongly suggest the occurrence of a secondary circulating flow, made possible by a chiefly collisional regime beneath the free surface.

Keywords Granular flow · Boundary effects · PIV · Rheological stratification · Avalanche · Debris-flow

1 Introduction

Granular media are involved in several geophysical flows, such as rock avalanches, snow avalanches and debris flows, characterized by the rapid motion of a solid phase in an ambient fluid. Though granular materials are composed of discrete particles, a continuum fluid dynamics approach (e.g. Savage 1979; Savage and Hutter 1991) is often adopted, especially for describing natural geophysical hazards at the field scale (e.g. Medina et al. 2008; Pirulli and Mangeney 2008; Delannay et al. 2017). Several experimental and theoretical efforts have been made for better describing the dynamics of granular mixtures (e.g. Tubino and Lanzoni 1993; GDR MiDi 2004; Jop et al. 2006; Sarno 2013; Sarno et al. 2013, 2014) and channelized granular flows (e.g. Taberlet et al. 2003; Jop et al. 2005; Martino and Papa 2008; Sarno et al. 2011a). However, a comprehensive understanding of the granular flow dynamics is still an open problem. It was observed that

✉ L. Sarno
lsarno@unisa.it;
<http://www.unisa.it/dipartimenti/diciv/lidam/en/index>

L. Carleo
lcarleo@unisa.it

M. N. Papa
mnpapa@unisa.it

P. Villani
p.villani@unisa.it

¹ Department of Civil Engineering, University of Salerno, Via Giovanni Paolo II, 132, 84084 Fisciano, Italy

² CUGRI, University Consortium for Research on Major Hazards, Via Giovanni Paolo II, 132, 84084 Fisciano, Italy

granular media basically exhibit three different flow regimes resembling the state of aggregation of matter (Forterre and Pouliquen 2008). In the solid-like regime, characterized by slow deformations and long-lasting contacts between grains, the main momentum flux mechanism is frictional. On the other hand, the grain-inertia regime, originally observed by Bagnold (1954), is characterized by inelastic collisions between grains and can be described by kinetic models, resembling the classical theory of gases (e.g. Goodman and Cowin 1972; Jenkins and Savage 1983; Lun et al. 1984; Armanini et al. 2008). Between these two extreme behaviours, there is an intermediate regime, frequent in geophysics and often referred to as *dense-collisional*, where the granular medium flows more like a fluid and frictional and collisional dissipation mechanisms occur simultaneously. This coexistence can be explained by the concurrence of force networks and clusters surrounded by these networks, where grains are free to collide (e.g. Radjai et al. 1996; Prochnow et al. 2000; Mills et al. 1999). The relative importance of collisions with respect to friction can be described by a dimensionless number, the inertial number, I (da Cruz et al. 2005), which is essentially the square root of the Coulomb number previously defined by Ancey et al. (1999). For a simple shear flow, it can be written as $I = \dot{\gamma}d/\sqrt{\sigma/\rho_s}$, where $\dot{\gamma}$ is the shear rate, d is the grain diameter, σ/ρ_s is the pressure, σ , normalized by the grain density, ρ_s .

The lack of a unified vision has motivated a number of theoretical models for describing the rheology in the dense regime. Savage (1984) assumed that the bulk stress tensor could be described as the sum of a Coulomb frictional term and a collisional term. Ancey and Evesque (2000) developed a model where the frictional and collisional contributions to the stress tensor depend on the Coulomb number. Based on the observations from both experiments and discrete element numerical simulations, GDR MiDi (2004) and Jop et al. (2006) devised an empirical $\mu(I)$ -rheology, where the shear stress τ is assumed to be proportional to the normal stress, σ , through a friction coefficient, μ , depending on the inertial number, I . Although the $\mu(I)$ -rheology is capable of capturing the global behaviour of dense granular flows (e.g. Jop et al. 2006), it cannot describe important features of their dynamics, e.g. the existence of different thickness-dependent angles of repose (Pouliquen 1999) and the occurrence of a lower slowly moving flow (Komatsu et al. 2001; Jop et al. 2005). Some alternative models, aiming at capturing non-local effects, due to force chains, have also been proposed (e.g. Mills et al. 1999; Pouliquen and Forterre 2009; Kamrin and Koval 2012). Recently, Kamrin and Henann (2015) employed their non-local theory, based on an additional state parameter called *granular fluidity*, to describe the

motion of granular material down inclined planes. This non-local model was found to be able to capture the relation between the stopping heights and the inclination angles, experimentally observed by Pouliquen (1999).

Despite these recent efforts, to date there is still no rheological model capable of fully describing several complex features of the dense regime, such as hysteresis, non-local effects, shear localization and boundary effects (e.g. Jop 2015; Delannay et al. 2017). Hence, besides theoretical studies, laboratory experiments still represent irreplaceable tools for better understanding the dynamics of granular flows. Today, a number of non-intrusive and cost-effective optical methods are available for measuring the flow velocity. The most popular ones are the particle tracking velocimetry, PTV (e.g. Capart et al. 2002; Jesuthasan et al. 2006), and the particle image velocimetry, PIV (e.g. Willert and Gharib 1991). PTV basically works by individually tracking visible particles along subsequent images in a Lagrangian way. Differently, PIV finds the most likely displacements, by employing the cross-correlation function of the image intensity field. This technique, broadly employed in fluid dynamics, has been recently extended also to granular flows (e.g. Lueptow et al. 2000; Eckart et al. 2003; Pudasaini et al. 2005; Pudasaini et al. 2007). Seeding with opaque particles is generally not required in PIV applications on granular flows, thanks to the natural optical patterns of the grain surfaces. Moreover, appropriate illumination systems, such as flashlight (Eckart et al. 2003; Pudasaini et al. 2005) or flickering-free LED light (Sheng et al. 2011), are usually employed, instead of the laser sheets used in standard PIV applications. Though PTV and PIV techniques can be only employed at the boundaries of the flow domain if the granular medium is non-transparent, both methods achieved a high degree of robustness for granular flow applications (e.g. Eckart et al. 2003; Jesuthasan et al. 2006).

In the last decades, several experimental studies on granular flows (e.g. Drake 1990; Ahn et al. 1991; Pouliquen 1999; Ancey 2001; Komatsu et al. 2001; Bonamy et al. 2002; GDR MiDi 2004; Taberlet et al. 2003, 2004; Jop et al. 2005; Sarno et al. 2011b; Baker et al. 2016) provided useful information on velocity profiles in typical geometries, such as channelized flows, heap flows and rotating drums. In the majority of the works, studying channelized flows on a rigid bed, the velocity profiles are found to exhibit either an approximately linear behaviour (e.g. Ancey 2001) or the so-called *Bagnold* scaling (e.g. Pouliquen 1999; GDR MiDi 2004), which is obtainable from the grain-inertia regime originally observed by Bagnold (1954) and goes like the flow depth with a power 3/2. Differently, investigations on heap flows (i.e. semi-infinite geometry) and in rotating drums, characterized by a no-slip basal kinematic boundary condition (KBC), typically

exhibit velocity profiles with a convex shape, composed of a lower exponential tail, called *creep flow*, and an upper linear profile, called *surface flow* (Komatsu et al. 2001; Bonamy et al. 2002; GDR MiDi 2004). Due to the heterogeneity and the seeming contradictoriness of the available experimental data, it is still controversial which conditions determine the occurrence of one profile instead of the others. Boundary effects due to the basal surface (e.g. Ahn et al. 1991) or due to side walls (Taberlet et al. 2003, 2004; Jop et al. 2005) are often signalled as possible culprits of these seeming contradictory findings.

Motivated by the lack of homogeneous studies of the aforementioned phenomena, in this paper we report an extensive laboratory investigation on steady channelized dry granular flows, where the effects of both the basal surface and the flow depth have been systematically studied on a homogeneous data set, obtained by using a unique granular medium made of acetal-polymeric beads and three different basal surfaces. The velocity measurements at the sidewall and at the free surface were obtained by using two high-speed cameras and the open-source PIV code, PIVlab (Thielicke and Stamhuis 2014).

The employment of different basal roughnesses allowed us to observe a comprehensive range of basal KBCs: namely, slip with weak grain rolling, no-slip without grain rolling and no-slip with grain rolling. As well, very diverse shapes of the sidewall velocity profiles have been observed. The sidewall velocity profiles, occurring in case of high enough flow depths, can be well described by recurring to appropriate composite functions, variously composed of the Bagnold, linear and exponential scalings. The composite nature of such profiles strongly suggests the occurrence of a rheological stratification along the flow depth. Moreover, it has been found that the evolution in shape of the velocity profiles is driven not only by the roughness of the basal surface but also by the flow depth. In fact, we discovered that the shape of the velocity profile can greatly change even in the presence of the same basal surface, by merely varying the flow depth. On the one hand, this experimental observation can be explained by the relevant influence of the resistances at the sidewalls, which increase with the flow depth (e.g. Taberlet et al. 2003; Jop et al. 2005). On the other hand, it also suggests that the effects of the bed roughness on the flow dynamics are mediated by the kinematics at the basal surface. In fact, such a shape transition of the velocity profile is found to be associated with the occurrence/inhibition of basal grain rolling, which is chiefly governed by the confining stresses at the bed and, thus, by the flow depth. The aforementioned findings, which to our knowledge have never been systematically observed before, represent a major contribution of this work.

The velocity measurements, taken at the free surface, exhibit an approximately parabolic shape with minima at the sidewalls, confirming that the sidewall resistances are non-negligible and that channelized granular flows have a clear three-dimensional character. In order to estimate the width-wise three-dimensional effects on the velocity field, an approximate approach, similar to that by Sheng et al. (2011) and consisting of a regularization of the sidewall velocity profiles by using the free-surface velocities, is proposed in Sect. 3.2.5. Finally, the joint information, coming from the normal-to-bed component of the sidewall velocities and from the transverse component of the free-surface velocities, strongly suggests the occurrence of a weak secondary circulating flow, spanning a thickness of few grain diameters beneath the free surface. Such a secondary circulation, which to our knowledge has never been investigated before, could be relevant to continuum modelling of granular currents and signals non-trivial influences of the rigid boundaries on the flow dynamics.

The paper is composed of the following parts: a description of the experimental apparatus and of the measurement techniques is reported in Sect. 2. The experimental results together with the related discussion are reported in Sect. 3. Finally, the main findings are summarized in Sect. 4.

2 Materials and Methods

2.1 Experimental Apparatus

Here, we briefly describe the experimental apparatus, where all experiments have been performed. It consists of a 2-m-long Plexiglas flume with a rectangular cross section of width $W = 0.08$ m corresponding to $\approx 24d$. The upper part of the channel, which is 50 cm long and is equipped with an external hopper, is used as a reservoir and has a capacity of ≈ 40 l. It is connected to the rest of the channel by a gate with an adjustable opening, located close to the bottom. The flume inclination, β , was set to 30° for all runs. The granular material is made of copolymer (POM) beads with mean diameter, $d = 3.3$ mm, and relative standard deviation of d equal to 5% (Sarno et al. 2011b, 2016). The angle of internal friction at constant volume, φ , was estimated $\approx 27^\circ$ by direct shear tests, performed on samples of size $10\text{ cm} \times 10\text{ cm} \times 4\text{ cm}$. The relevant physical properties of the granular material are reported in Table 1.

So as to investigate different KBCs at the bed, the following three basal surfaces were employed:

1. smooth Bakelite surface (hereafter identified with the symbol S),

Table 1 Properties of the granular material

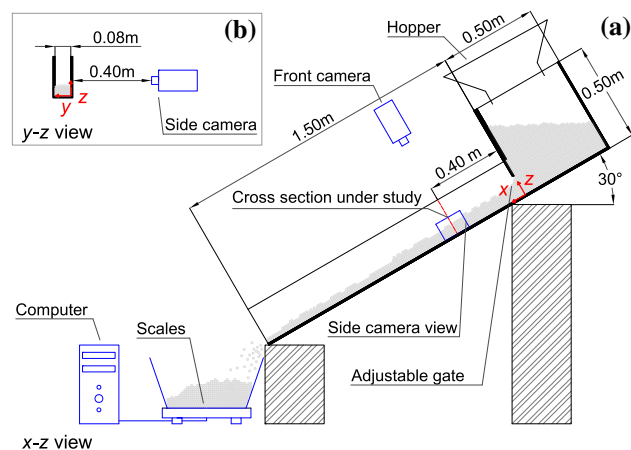
Parameter	Value
Chemical composition	Polyoxymethylene
Mean diameter, d	3.3 mm
Relative standard deviation of d	5%
Grain density, ρ_s	1410 kg/m ³
Young's modulus	2700 MPa
Poisson ratio	0.35
Volume fraction at deposit	0.63
Internal angle of friction, φ	27°
Coefficient of restitution	0.83

- roughened surface (identified with G), obtained by randomly gluing a layer of POM grains on the Bakelite surface,
- sandpaper surface (identified with R) with average characteristic length of the roughness equal to 425 μm .

The angle of friction between the surface G and the granular medium is equal to φ . To measure the angles of friction between surfaces S and R , and the granular material, we followed the approach proposed by Savage and Hutter (1991). A small amount of grains, confined in a small cylindrical container, was let flow down an incline covered by the investigated surfaces. The angle of friction was determined as the minimum angle at which the sample flowed down the incline without acceleration. This estimation can be regarded as a lower bound of the effective angle of friction, which is expected to slightly increase with the slip velocity (e.g. Jop et al. 2005; Artoni et al. 2009; Artoni and Richard 2015). We found 14.5° for the Bakelite surface and 34° for the sandpaper. Similarly, the angle of friction between the Plexiglas walls and the granular material was found equal to 19.5°. These measurements have shown a standard deviation of $\approx 1^\circ$.

An electronic scale (load cell mod. LaumasAZL-50 kg) with resolution of 1 g and accuracy of ≈ 8 g, was placed at the flume outlet for measuring the mass flow rate. Considering an orthogonal frame of reference ($Oxyz$) with the x -axis aligned with the down slope direction and the origin O located at the gate, the laboratory apparatus is sketched in Fig. 1.

The granular flow was video recorded at the investigated cross section, located 40 cm downstream the gate, by two high-speed digital cameras (mod. AOS S-PRI and AOS Q-PRI) with a sampling rate of 1 kHz. The camera, S-PRI, was placed aside the channel; the other one was located above the channel to capture the motion at the free surface. A high-intensity flickering-free LED lamp (mod. Photo-Sonics MultiLED-LT, ≈ 8000 lm) was placed aside the

**Fig. 1** Sketch of the experimental apparatus: **a** x - z view; **b** Inset y - z view

cross section under study. The lamp position was adjusted before each test, so as to point around 1 cm above the free surface. In this way, one single lamp allowed a suitable illumination of both the sidewall and the free surface. For proper image exposure, the shutter times were chosen equal to 50 and 200 μs for the side and the front camera, respectively.

2.2 Description of the Experimental Campaign

Before each run, the gate opening was carefully adjusted and a mass of ≈ 30 kg of granular material was loaded into the upper reservoir. Then, the gate was opened by manually removing a front shutter. Different from fluids, the flow rate through an aperture depends weakly on the level of granular medium in the reservoir (e.g. Nedderman et al. 1982). It allowed us to obtain a substantially steady flow in an intermediate time window for all experiments. A preliminary check of it was carried out for each combination of gate opening and basal surface, by recording a footage of the entire flow through the sole side camera with a slower sampling rate of 100 Hz. A simple code, written in MATLAB and based on image binarization, allowed us to estimate the level of the free surface, z_f , from the bottom surface, with pixel accuracy (i.e. $\approx 2 \times 10^{-4}$ m). For all the investigated gate openings, from 5 to 14 cm, the steady state was always observed in a time interval of several seconds. As an example, the cumulated weights at the flume outlet and the free-surface evolution, measured in this preliminary run of experiment Exp-12S (corresponding with a gate opening of 12 cm and bed surface S), are shown in Fig. 2. From Fig. 2, it is visible that the flow is steady on average in a time window between $t = 3$ s and $t = 9$ s for this run.

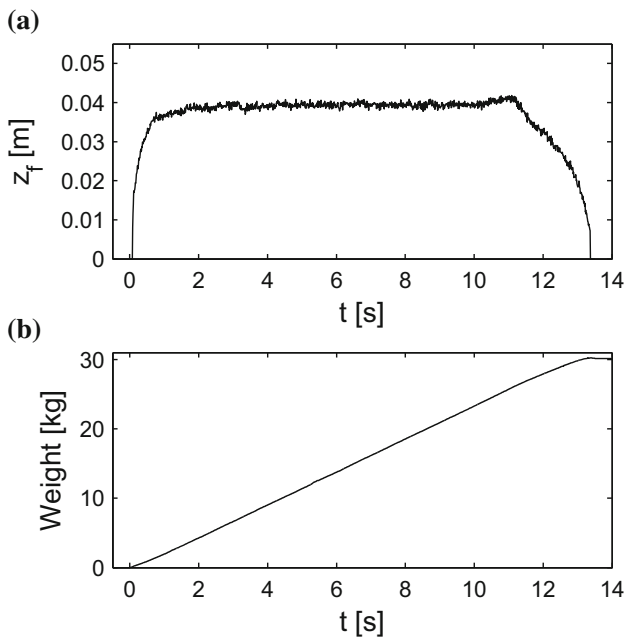


Fig. 2 Preliminary test of Exp-12S: **a** evolution of the flow thickness. **b** Cumulated weight measured at the chute outlet

After these preliminary checks, each experiment was repeated four times, so as to statistically treat all the measurements. In each of these runs, the steady flow was recorded at 1 kHz for subsequent PIV analysis. The complete list of 21 experiments is reported in Table 2, where

the naming of the experiments is chosen so as to give information about the upstream gate opening and the type of bed surface (e.g. Exp-5S means gate opening set to 5 cm and S-type bed). All the flows were not far from the fully developed uniform state. In fact, in the entire data set the inclination of the free surface with respect to the bottom, $\beta' = \arctan(-\partial_x h)$, was found to be very small at the investigated cross section ($x = 0.40$ m), compared to the inclination of the channel ($\beta = 30^\circ$). The mass flow rate, Q_m , at the outlet, the flow thickness, z_f , the inclination of the free surface, β' , and the aspect ratio, $\varepsilon = z_f/W$ at the investigated cross section, are shown in Table 2. Since the flow is steady on average, all the measurements, reported in Table 2, are time averages, obtained by averaging data over time intervals of 1 s (taken within the steady-state interval) in each repetition and, then, by further averaging over the four repetitions. The experimental repeatability was tested through the relative standard deviation (*rsd*), obtained for each experiment on the four repetitions: the mass flow rates from different repetitions scatter around their average with a typical *rsd* of 2.5%. As well, z_f is found to have a very small *rsd* of 1.2%. The plots of the mass flow rates, Q_m , against z_f on different surfaces are reported in Fig. 3.

As shown in Fig. 3, for a given z_f the runs on surface S exhibit a much larger Q_m than the runs on surfaces G and R. This is due to the much lower basal friction on surface S.

Table 2 Complete list of experiments

Run	Gate opening (m)	Basal surface	Q_m (g s ⁻¹)	z_f (x = 0.40 m) (m)	ε	β' (°)
Exp-5S	0.05	Bakelite (S)	926	0.0133	0.17	0.30
Exp-6S	0.06	Bakelite (S)	1181	0.0183	0.23	0.73
Exp-7S	0.07	Bakelite (S)	1402	0.0204	0.26	0.80
Exp-8S	0.08	Bakelite (S)	1622	0.0239	0.30	1.39
Exp-10S	0.10	Bakelite (S)	1994	0.0316	0.40	1.61
Exp-12S	0.12	Bakelite (S)	2466	0.0396	0.50	2.02
Exp-14S	0.14	Bakelite (S)	2845	0.0465	0.58	1.97
Exp-5G	0.05	Grain (G)	309	0.0397	0.50	0.24
Exp-6G	0.06	Grain (G)	387	0.0461	0.58	0.02
Exp-7G	0.07	Grain (G)	495	0.0511	0.64	0.72
Exp-8G	0.08	Grain (G)	577	0.0589	0.74	0.66
Exp-10G	0.10	Grain (G)	784	0.0693	0.87	0.89
Exp-12G	0.12	Grain (G)	1016	0.0803	1.00	1.04
Exp-14G	0.14	Grain (G)	1257	0.0894	1.12	0.94
Exp-5R	0.05	Sandpaper (R)	643	0.0223	0.28	-0.44
Exp-6R	0.06	Sandpaper (R)	755	0.0367	0.46	0.08
Exp-7R	0.07	Sandpaper (R)	837	0.0437	0.55	0.47
Exp-8R	0.08	Sandpaper (R)	928	0.0507	0.63	0.49
Exp-10R	0.10	Sandpaper (R)	1041	0.0608	0.76	0.78
Exp-12R	0.12	Sandpaper (R)	1208	0.0703	0.88	1.44
Exp-14R	0.14	Sandpaper (R)	1488	0.0793	0.99	1.66

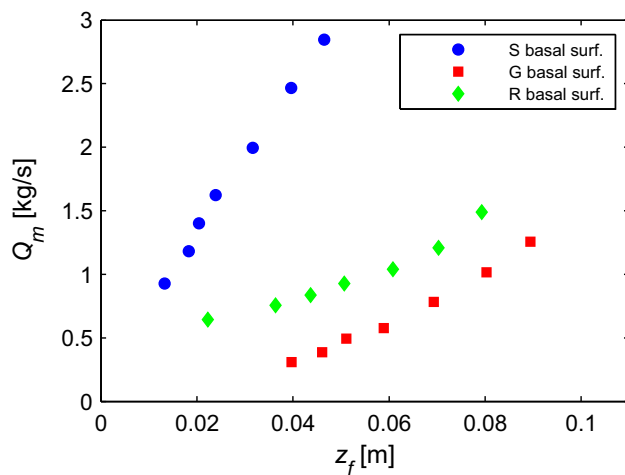


Fig. 3 Plots of the mass flow rates, Q_m , as function of the flow thickness, z_f , on different basal surfaces

Interestingly, the values of Q_m observed on surface R approach the ones observed on surface S in case of small flow depths, while they tend to the ones observed on surface G when z_f increases. This behaviour is clearly linked with the different KBC enforced by the bed roughness and in particular with the occurrence of slip or no-slip conditions. Following Ahn et al. (1991), with the expression “slip KBC” here we mean a relative tangential sliding of the grains and the bed surface. According to this definition, non-null velocities of the grains at the basal surface do not necessarily imply a slip KBC, since the centre of mass of grains may move also because of grain rolling. A naked-eye analysis of the images from the side camera allowed us to verify the occurrence of a strong relative sliding between the grains and the S -type bed surface (slip KBC), and weak rolling. On the contrary, no-slip KBC was observed on the R -type and G -type surfaces. However, a regular particle rolling was observed at the surface R in the tests with low flow depths, while this phenomenon was found to gradually subside with increasing z_f . We anticipate that such a basal rolling of particles, made possible thanks to the small characteristic length of roughness of surface R ($425 \mu\text{m}$), compared to the grain diameter (3.3 mm), has a crucial influence also on the shape of the velocity profiles, as it will be shown in Sect. 3.2.3.

2.3 Velocity Measurements Through Particle Image Velocimetry (PIV)

Here, we briefly recall the principles of the PIV technique and report the details of the granular PIV analyses, carried out in this work. PIV algorithms basically work by calculating the cross-correlation function of the image intensity

field between two consecutive images, taken in a time interval, Δt . Each image is divided into sub-regions, called *interrogation windows*. For each interrogation window, Γ , the following optimization problem is solved

$$\max_{\mathbf{d}} \int_{\Gamma} f(\mathbf{r}) g(\mathbf{r} + \mathbf{d}) dA, \quad (1)$$

where \mathbf{r} is the position vector, \mathbf{d} is the displacement vector to be varied in the optimization task, f and g are the image intensity fields at t and $t + \Delta t$. The maximum of the correlation function in (1) corresponds to the most likely displacement, \mathbf{d} . The open-source code, PIVlab, used in this work and already employed in various fluid dynamics and granular flow applications (e.g. Sanchez et al. 2012; Jiang and Towhata 2013; Baker et al. 2016), is based on a window displacement multi-step algorithm (e.g. Scarano and Riethmuller 2000), showing a good robustness even in presence of high-velocity gradients, which is typical in granular flows. The problem (1) is solved by PIVlab in the frequency domain through a fast Fourier transform. Sub-pixel accuracy is achieved by a three-point Gauss interpolation along two normal directions. The typical random error of PIVlab is ≈ 0.02 pixel/frame, as reported by Thielicke and Stamhuis (2014). Considering the length scales and the frame rate (1 kHz) employed in the present experimental investigation, the expected PIV accuracy is $\approx 0.004 \text{ m/s}$ for the sidewall measurements and $\approx 0.002 \text{ m/s}$ for the measurements at the free surface. However, we signal that the PIV accuracy could be slightly worse, closest to the free surface, since the PIV measurements could be slightly influenced by the fluctuation of the free-surface level. All the PIV analyses were performed on partly overlapping image pairs, so as to get 1000 measurements per second. Images from the side camera were analysed by using four passes, with 50% overlapping interrogation windows of sizes 64, 32, 16, 8 pixels. To get the same spatial resolution, the images from the front camera were analysed by using three PIV passes with interrogation windows of sizes 64, 32, 16 pixels. Considering that the particle diameter, d , is ≈ 16 pixels and ≈ 32 pixels in the side and front images, respectively, the obtained PIV spatial resolution is $d/2$. Though such a fine resolution might appear unnecessary due to the discrete nature of grains, we found convenient to keep it, so as to reduce as much as possible the spatial averaging errors near the free surface.

3 Results and Discussion

3.1 Description of Instantaneous and Time-Averaged Velocities

The non-processed instantaneous PIV measurements and the subsequent time-averaging procedure are here

presented in detail for the only experiment, Exp-10G. The results, reported in this section, are useful also for anticipating some features of the velocities profiles, common to the rest of the investigated data set. The time-averaged velocity profiles of all the experiments will be shown in Sect. 3.2.

The x - and z -components of the time-averaged sidewall flow velocities of Exp-10G are reported in Fig. 4, together with the related standard deviations and the instantaneous measurements (*raw data*). The time-averaged velocity profiles, denoted by an overbar, are obtained by averaging the instantaneous velocities over a time interval of 1 s. It was preliminary observed that averages over longer time intervals did not yield significantly different results. As one can see from Fig. 4a, $\bar{u}_x(z)$ is a strictly increasing function and is chiefly convex (i.e. $\partial_{zz}\bar{u}_x \geq 0$). This velocity profile is in agreement with other experimental works available in the literature (e.g. Komatsu et al. 2001; Bonamy et al. 2002; GDR MiDi 2004) and common to all other experiments on surface G of the present investigation (cf. Sect. 3.2). Following GDR MiDi (2004), such a kind of

velocity profile can be regarded as composed of two different parts: in the upper zone, often called *surface flow*, the profile is approximately linear, while an exponential tail develops in the lower zone, often called *creep flow* (Komatsu et al. 2001). This two-component behaviour strongly suggests the occurrence of a frictional-collisional rheological stratification along the flow depth, which is driven by gravity and may be described by a two-layer depth-averaged model (e.g. Doyle et al. 2010; Sarno et al. 2014, 2017). According to this interpretation, the main dissipative mechanisms in the creep flow are of frictional type, while frictional-collisional momentum exchanges take place in the faster upper layer. This stratification is also reminiscent of that observed in granular mixtures with dense ambient fluid (Armanini et al. 2005, 2009), where additionally the fluid viscosity plays a crucial role in determining the location of the interface between the layers. It is worth mentioning that in channelized dry granular flows the development of such a stratification, and the consequent convex-shaped velocity profile, is promoted by the frictional resistances exerted at the side walls, as experimentally observed by Taberlet et al. (2003) and described through a $\mu(I)$ -rheology by Jop et al. (2005). In order to explain the crucial effects of the sidewalls, a generalization of the approach proposed by Jop et al. (2005), which avoids the assumption of a specific rheological law, is reported in “Appendix”. This argument facilitates a physical interpretation of the occurrence of non-concave regions (i.e. $\partial_{zz}\bar{u}_x \geq 0$) in the velocity profiles, and it will be used in the following sections for interpreting some features of the experimental results.

Let us discuss now the z -component velocity profile (Fig. 4b). Though \bar{u}_z is much smaller ($\approx 1\%$) than \bar{u}_x , owing to the shallow nature of the flow, the \bar{u}_z profile reveals interesting information about the flow regime, especially as regards mass and momentum fluxes along the flow depth. As expected, at the free surface $-\bar{u}_z/\bar{u}_x$ is equal to the slope of the free surface, $\tan \beta'$, and tends to a null value at the rigid bed according to the KBC there. Interestingly, the minimum of \bar{u}_z is not at the free surface but around $4d$ below it. This observation is not accidental, since analogous trends were observed in the majority of experiments hereafter reported. The \bar{u}_z -profile reveals that, on average, the grains near the sidewall tend to move downwards, driven by gravity and that this continuous *fall* of grains is not compensated by the upward rebounds due to collisions. This trend is probably made possible by the small values of the solid volume fraction beneath the free surface, allowing the grains to fall down the holes, which occasionally form due to shearing. Conversely, the phenomenon fades away at depths greater than $4d$, probably due to an increase of the solid volume fraction. To the

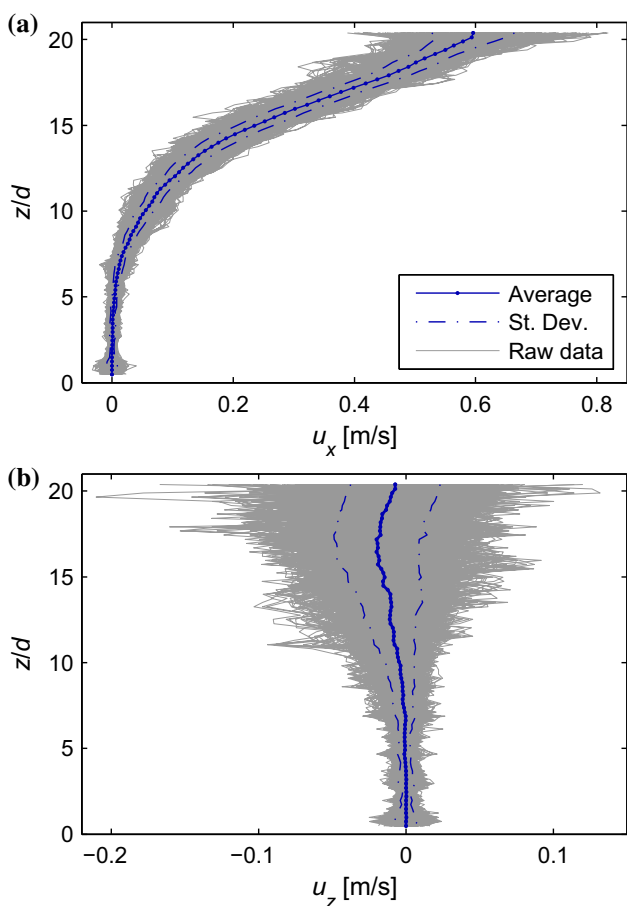


Fig. 4 Instantaneous (Raw data) and time-averaged (Average) sidewall velocity profiles (Exp-10G) with the related standard deviations (St. Dev.): **a** x -component, **b** z -component

authors' knowledge, this finding has never been observed nor signalled in other experimental works available in the literature and deserves further investigation, possibly with additional measurements of the solid volume fraction along the flow depth.

The standard deviations of u_x and u_z typically increase with z , due to an increase in grain collisions. A similar trend was also observed in the other tests on surfaces G and R, as it will be shown hereafter (cf. Figs. 6, 8, 9). The average standard deviation of \bar{u}_x is 0.019 m/s, while that of \bar{u}_z is 0.014 m/s. The standard deviations at the free surface are much larger, 0.065 for \bar{u}_x and 0.025 m/s for \bar{u}_z . Yet, it should be kept in mind that some additional PIV errors could arise in measurements, closest to the free surface, due to the fluctuation of the free-surface level.

The instantaneous and time-averaged PIV measurements, taken at the free surface, are reported in Fig. 5. The profile of $\bar{u}_x|_{z_f}$ (Fig. 5a) is symmetric and exhibits an approximately parabolic shape with a maximum at $y = W/2$

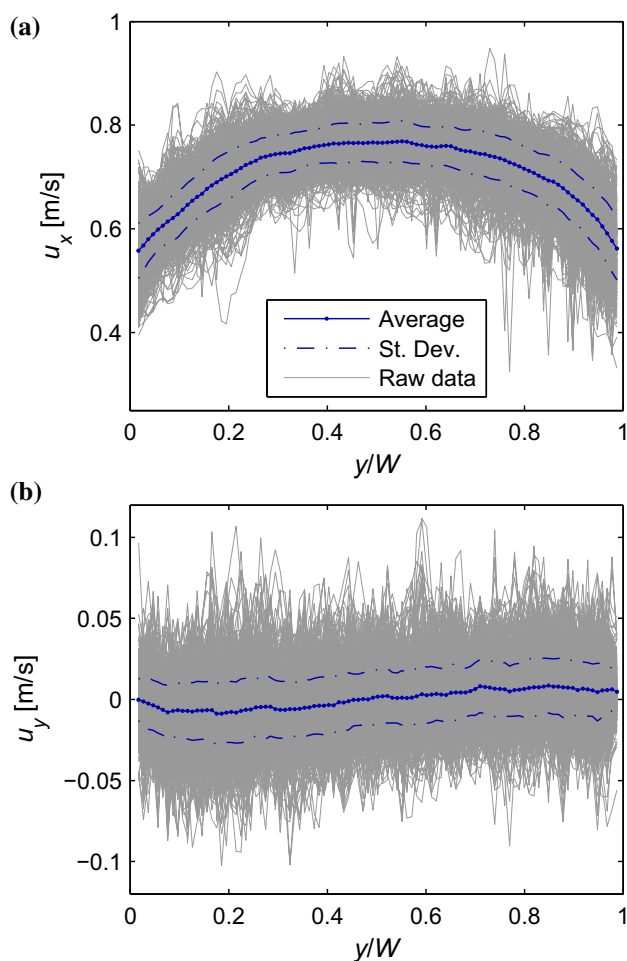


Fig. 5 Instantaneous (Raw data) and time-averaged (Average) free-surface velocity profiles (Exp-10G) with the related standard deviations (St. Dev.): **a** x -component, **b** y -component

and the minima at the side walls. This profile, which is qualitatively in agreement with other several experimental works (e.g. Jop et al. 2005; Baker et al. 2016), confirms the non-negligible influence of the resistances at the side walls. Differently, $\bar{u}_y|_{z_f}$, which is much smaller than $\bar{u}_x|_{z_f}$, exhibits an anti-symmetric shape with approximately null values at $y = W/2$ and at the side walls, owing to the KBCs there (Fig. 5b). Such a spread of grains is due to grain collisions, which tend to scatter the linear momentum along the cross section in a turbulent-like fashion. The $\bar{u}_y|_{z_f}$ profile, together with the sidewall profile of \bar{u}_z (Fig. 4b), is compatible with the occurrence of a weak secondary flow beneath the free surface. According to this interpretation, as the observed flows are not far from the uniform state, a certain amount of grains are expected to go up to the free surface in the middle of the flume ($y \approx W/2$), probably driven by stronger collisions, in order to fulfil the mass balance within the cross section.

3.2 Ensemble-Averaged Measurements of Flow Velocities, Shear Rate and Granular Temperature

The velocity measurements, reported in this section, were obtained from the ensemble averages over four repetitions of the same experiment, in which the velocities were previously time-averaged over a time interval of 1 s in each repetition. The time-averaged velocity profiles from different repetitions showed a standard deviation of ≈ 0.01 m/s, with respect to the ensemble average, and a *rsd* of $\approx 5\%$, which confirms the good experimental repeatability. As well, the velocity fluctuations along z exhibit very similar trends among the four repetitions, which further confirms the good repeatability.

From the sidewall velocity profiles, the shear rate, $\dot{\gamma}$, and the granular temperature, T , were estimated. Since the motion is prevalently in the x -direction, we can approximately assume that the shear rate is one dimensional (i.e. confined in the x - z plane). Hence, $\dot{\gamma}$ has been calculated from the \bar{u}_x velocity profile, by using the central difference approximate formula

$$\dot{\gamma}(z) = \partial_z \bar{u}_x(z) \approx \frac{\bar{u}_x(z + \Delta z) - \bar{u}_x(z - \Delta z)}{2\Delta z}, \quad (2)$$

where $\Delta z \approx 8 \times 10^{-4}$ m, according to the PIV resolution. At the free surface and at the bed, backward and forward difference approximate formulas were used, instead.

The granular temperature, T , similar to the thermodynamic temperature, is a scalar quantity representative of the specific kinetic energy of the grain particles. Different definitions of it can be given, depending on how many terms (e.g. translational, rotational, vibrational) are taken

into account. Here, we only consider the translational specific kinetic energy (Savage 1998). Therefore, T can be defined as follows

$$T(z) = \frac{1}{3} \sum_{i=1}^3 \langle (u'_i)^2 \rangle, \tag{3}$$

where the symbol $\langle \rangle$ represents the ensemble average operator and $(u'_i)^2$ is the square of the fluctuation velocity in i -direction, which is defined as $u'_i = u_i - \langle u_i \rangle$ according to the Reynolds decomposition. While there are PIV measurements of $(u'_x)^2$ and $(u'_z)^2$, $(u'_y)^2$ is unknown. Therefore, similar to Jesuthasan et al. (2006), we assumed that $\langle (u'_y)^2 \rangle \approx \langle (u'_z)^2 \rangle$, thus, (3) is recast

$$T(z) \approx \frac{\langle (u'_x)^2 \rangle + 2\langle (u'_z)^2 \rangle}{3}. \tag{4}$$

By assuming also that the statistically stationary system under study is ergodic, the ensemble averages in (4) are equivalent to the corresponding time averages, i.e. $\langle (u'_i)^2 \rangle \approx \overline{(u'_i)^2}$. Consequently, such quantities have been estimated here by time-averaging the squares of the PIV fluctuation velocities over a time interval of 1 s. Analogous to that done for the velocity profiles, the T profiles have been subsequently averaged over all four repetitions available for each experiment. It should be kept in mind that also errors, due to the PIV technique, are injected into the velocity fluctuations of (4). However, since the random PIV errors at the sidewall are of order of ≈ 0.004 m/s and the fluctuations, due to the flow dynamics, are much greater (of order of 0.02 m/s on surfaces R and G and are even greater on surface S), the relative error in estimating T is typically smaller than 4%.

3.2.1 Sidewall Measurements: Experiments on Surface S (Smooth Bed)

The plots of \bar{u}_x , \bar{u}_z , $\dot{\gamma}$ and T , related to experiments on the smooth bed surface S , are reported in Fig. 6. All the \bar{u}_x -profiles exhibit a strictly increasing trend with z and non-null velocities close to the bottom surface, owing to the small wall-particle angle of friction enforcing a slip KBC. Analysing the $\dot{\gamma}$ -profiles of Fig. 6c, it is evident that in all runs $\dot{\gamma}$ reaches its maximum near the bed within a layer of thickness $\approx 1d$. This behaviour is due to the fact that the basal angle of friction, much smaller than the internal angle of friction, ϕ , causes the formation of a shear band (e.g. Shojaee et al. 2012). A discussion on the flow dynamics at the basal surface is postponed to the end of this section. In the middle region of the flow, $\dot{\gamma}$ is approximately constant,

$\dot{\gamma} \approx 20 \text{ s}^{-1} \approx 0.4\sqrt{g/d}$. This value is of the same order as the averaged shear rates, observed in several other experiments in similarly narrow geometries (e.g. GDR MiDi 2004). Moreover, in all runs on S-type bed, $\dot{\gamma}$ is found to decrease within a layer of thickness $\approx 2.5d$, close to the free surface.

The result is that the \bar{u}_x profiles (cf. Fig. 6a) exhibit three different regions, from the bottom to the top: a $1d$ -thick basal shear band, an approximately linear intermediate zone with variable thickness, which tends to vanish in runs with small flow depths, and, finally, an upper concave zone ($\partial_{zz}\bar{u}_x < 0$) with thickness of $\approx 2.5d$. Such a concave shape of the velocity profile in the upper zone suggests a prevalently collisional behaviour (Bagnold 1954).

Firstly, we tried to describe the velocity profiles through a unique curve fitting along the whole flow depth. To do so, we employed both the Bagnold and the linear scalings. For the Bagnold scaling, we used the function

$$\bar{u}_x(z) = a_{\text{Bag}} + b_{\text{Bag}} \left[z_f^{3/2} - (z_f - z)^{3/2} \right], \tag{5}$$

where the parameters a_{Bag} and b_{Bag} have been optimized over the entire velocity profile except the measurements in the shear band, which cannot be correctly described by Eq. (5). From a physical viewpoint, a_{Bag} represents the best-fitting estimate of the basal slip velocity and b_{Bag} , according to the grain-inertia Bagnoldian regime, is a function of the bulk density, ρ_s , of the grain diameter, d , and of the solid volume fraction, c . The scaling of Eq. (5) is obtainable, under the hypothesis of infinitely large channel, from the Bagnold grain inertial regime (Bagnold 1954), where the shear stress, τ , is a quadratic function of $\dot{\gamma}$

$$\tau = \rho_s f(c) d^2 \dot{\gamma}^2, \tag{6}$$

with $f(c)$ being a function of the solid volume fraction, c . According to the Bagnold theory, the momentum flux mechanisms are expected to be chiefly collisional, if Eq. (6) holds. However, it should be noted that the Bagnold rheology is of more general validity, since a rheological relation, $\tau \propto \dot{\gamma}^2$, similar to Eq. (6), can be also derived through dimensional analysis by merely assuming that the prevalent timescale of the granular system is the inverse of $\dot{\gamma}$ (e.g. Silbert et al. 2003). Moreover, it is worth mentioning that an analogous scaling of Eq. (5) comes out also from the $\mu(I)$ -rheology (e.g. Jop et al. 2005, 2006), when the $\mu(I)$ constitutive law is integrated in the absence of sidewall resistances and under the assumption that the normal and the shear stresses linearly increase with the distance from the free surface.

As regards the linear curve fitting, we employed the function

$$\bar{u}_x(z) = a_1 + b_1 z. \tag{7}$$

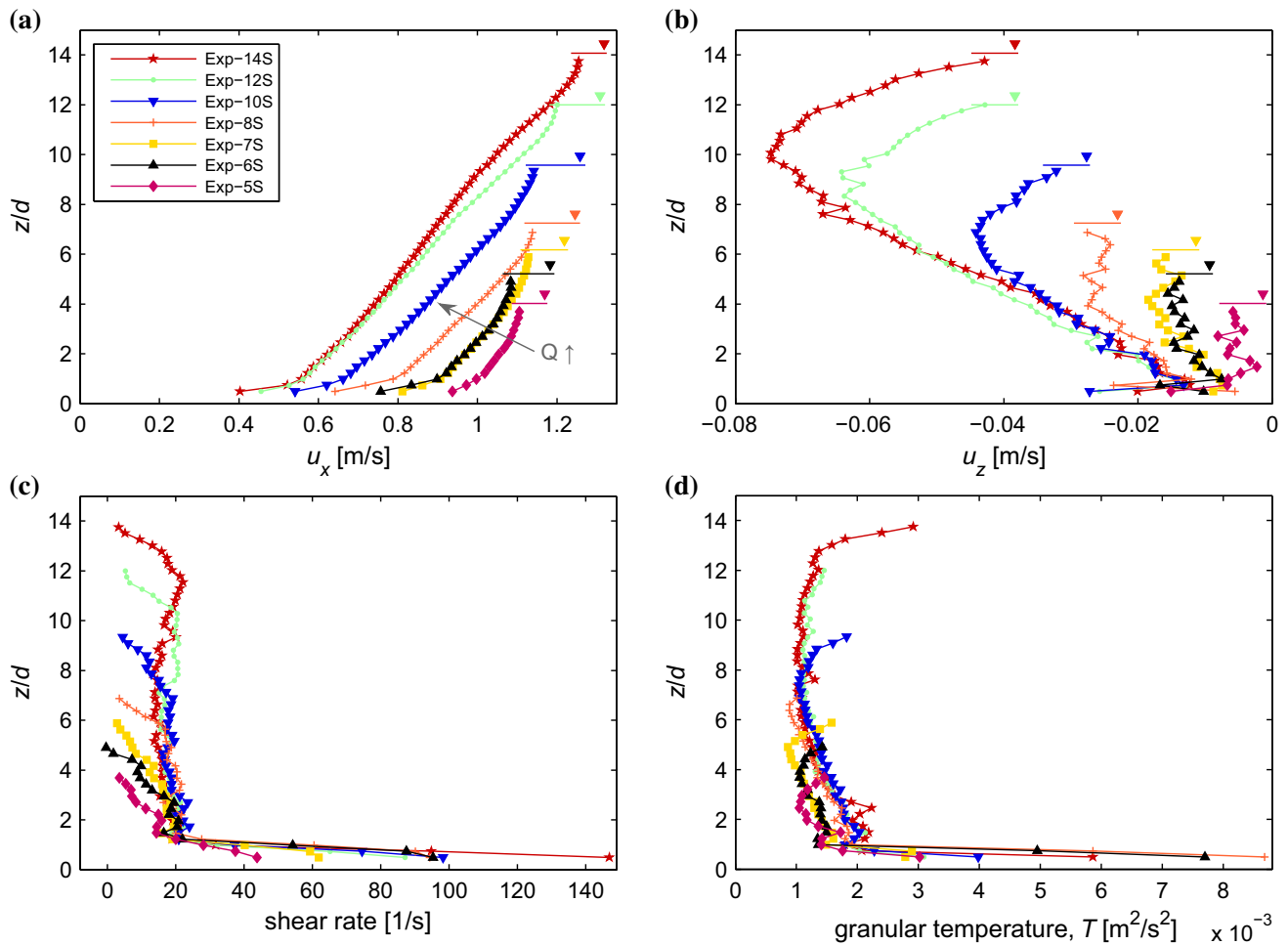


Fig. 6 Sidewall velocity profiles of experiments on smooth surface S (averages on 4 repetitions), **a** x -component, **b** z -component, **c** shear rate, **d** granular temperature

Also, in this case, the velocity measurements within the shear band were neglected for the parameter optimization. The best-fitting parameters of Eqs. (5) and (7) are summarized in Table 3, together with the coefficients of determination, R^2 .

Although no constraint has been imposed on the fitting parameters a_{Bag} and a_1 , Table 3 shows that these values,

representing the slip velocity predicted by the two models, are quantitatively comparable to the PIV velocities closest to the basal surface (Fig. 6a). As shown in Table 3, the \bar{u}_x profiles of experiments with relatively small flow depths (Exp-5S, Exp-6S and Exp-7S) are well fitted by the Bagnold model (5). Differently, as the flow depth increases, the Bagnold fit worsens and the linear fit appears more and more suitable to capture the main trend of the velocity

Table 3 Best-fitting parameters of the Bagnold (5) and linear (7) models for the sidewall velocity profile on surface S

Run	Bagnold model			Linear model		
	a_{Bag} (ms^{-1})	b_{Bag} ($\text{m}^{-1/2}\text{s}^{-1}$)	R^2	a_1 (ms^{-1})	b_1 (s^{-1})	R^2
Exp-5S	0.943	121.2	0.998	0.980	11.11	0.965
Exp-6S	0.829	125.9	0.998	0.877	14.12	0.963
Exp-7S	0.836	109.5	0.999	0.884	13.85	0.971
Exp-8S	0.688	128.7	0.994	0.752	18.20	0.993
Exp-10S	0.557	104.6	0.994	0.630	17.73	0.993
Exp-12S	0.435	90.78	0.978	0.514	17.95	0.999
Exp-14S	0.441	76.68	0.970	0.517	16.41	0.998

Table 4 Best-fitting parameters of the composite fit, made up of the lower linear model, (7), and of the upper Bagnold model (8), together with the normalized depths of both layers, h_1/d and h_2/d

Run	Lower linear model			Upper Bagnold model			h_1/d	h_2/d
	$a_{1,1}$ (ms ⁻¹)	$b_{1,1}$ (s ⁻¹)	R^2	$\bar{u}_x _{z=h_1}$ (ms ⁻¹)	$b_{\text{Bag},2}$ (m ^{-1/2} s ⁻¹)	R^2		
Exp-8S	0.737	19.78	0.999	1.055	161.3	0.999	4.90	2.34
Exp-10S	0.613	19.17	0.998	1.042	133.9	0.999	6.87	2.45
Exp-12S	0.516	17.77	0.999	1.069	158.8	0.998	12.00	2.69
Exp-14S	0.528	15.76	0.998	1.100	164.4	0.998	10.80	2.95

profile. Yet, the linear model (7) obviously cannot correctly describe the thin concavity, observed near the free surface.

Two probable physical interpretations of these experimental findings are proposed here. Firstly, the influence of the resistances exerted at the sidewall clearly becomes more and more important with the distance from the free surface (“Appendix”). As observed by Jop et al. (2005), such resistances typically reduce the concavity of the velocity profiles and are capable of making the profiles even convex, as it is slightly visible in the middle zone of the velocity profiles of Exp-12S and Exp-14S (cf. Fig. 6a). Secondly, as the flow depth increases, force chains among grains (e.g. Mills et al. 1999; da Cruz et al. 2005; Kamrin and Koval 2012; Jop 2015) are likely to develop, owing to larger confining pressures and the consequently greater number of long-lasting contacts among grains. Such force chains, whose extent can be much larger than the grain diameter (e.g. Radjai et al. 1996), introduce non-local effects in the momentum exchange mechanisms, which could be responsible for the shift from the Bagnold to a linear scaling. Mills et al. (1999) proposed a non-local constitutive law, which predicts dominantly linear velocity profiles with a weak concavity (i.e. $\partial_{zz}\bar{u}_x < 0$) in the vicinity of the free surface. Such theoretical profiles are qualitatively in agreement with those observed in the present experimental investigation. The coexistence of a thin concave layer beneath the free surface, suggesting a chiefly collisional Bagnold regime there, is not in contradiction with the aforementioned interpretation and can be explained by the fact that the effects of both the sidewalls resistances (Jop et al. 2005) and the force chains tend to vanish close to the free surface (Mills et al. 1999), owing to lower values of normal stresses and solid volume fraction.

To better describe the regime stratification occurring in the velocity profiles with large flow depths (i.e. in experiments from Exp-8S to Exp-14S), we tried a slightly more sophisticated model, composed of two superimposed fitting functions, $\bar{u}_{x,1}$ and $\bar{u}_{x,2}$, separated by an interface. The lower layer, denoted by the symbol “1” and having a thickness h_1 , is described through the linear model (7), while the upper layer, 2, spanning from the interface $z = h_1$ up to the free surface and having a thickness $h_2 = z_f - h_1$, is captured by the Bagnold model,

$$\bar{u}_{x,2}(z) = \bar{u}_x|_{z=h_1} + b_{\text{Bag},2} \left[(z_f - h_1)^{3/2} - (z_f - z)^{3/2} \right]. \quad (8)$$

The best-fitting parameters of the stratified model are reported in Table 4, together with R^2 and the depths, h_1 and h_2 , of the two layers. The difficulty in the estimation of the best-fitting parameters clearly lies in the uncertainty in identifying the interface. The possible locations of the interface along the flow depth were investigated in a discrete way by using the same spatial discretization, Δz , of the experimental velocity profiles. No constraints on the continuity of the composite function and on its derivative were imposed at the interface, so that it was possible to employ the following criterion. By varying the guessed interface location, we preliminary selected all the best-fitting composite profiles, which exhibit a velocity jump at the interface, $|\bar{u}_{x,1} - \bar{u}_{x,2}|$, smaller than a threshold (set equal to 0.01 m/s in the present analysis); subsequently, we chose the interface location, corresponding to the best fit that yields the minimum jump of the derivatives at the interface, $|\partial_z \bar{u}_{x,1} - \partial_z \bar{u}_{x,2}|$.

Comparisons among experimental data and the best curve fittings, reported in Tables 3 and 4, are shown in Fig. 10a.

The z -component of the flow velocities is everywhere negative along z (Fig. 6b). Analogous to that already reported in Sect. 3.1, in runs Exp-8S Exp-10S, Exp-12S and Exp-14S, \bar{u}_z exhibits the minimum at $\approx 4d$ from the free surface. This behaviour is less evident in runs Exp-5S, Exp-6S and Exp-7S, where \bar{u}_z is everywhere very small. This finding supports the existence of gravity-driven mass and momentum fluxes along z in the upper region of the flow close to the sidewall. As anticipated in Sect. 3.1, this observation, joined with the measurements at the free surface (cf. Fig. 11), strongly suggests the existence of a weak secondary circulating flow beneath the free surface. The mainly collisional regime beneath the free surface, pointed out by the concave shape of the \bar{u}_x profiles (cf. Fig. 6a), is likely to be associated with lower values of the volume fraction. It is worth noting that such a probable decrease in the volume fraction near the free surface also allows the mass fluxes along z -direction (i.e. the negative values of \bar{u}_z) that are necessary for the aforementioned secondary circulation to occur.

All the granular temperature profiles (Fig. 6d) exhibit a C-shaped trend, with relative maxima at the basal surface ($\approx 3 - 8 \times 10^{-3} \text{ m}^2/\text{s}^2$) and at the free surface ($\approx 2 - 3 \times 10^{-3} \text{ m}^2/\text{s}^2$), and an intermediate region with an approximately constant value ($\approx 1 \times 10^{-3} \text{ m}^2/\text{s}^2$). By comparing $\dot{\gamma}$ and T profiles, note that the maximum of T is located within the basal shear band, which is expected as the localized shear band causes strong grain fluctuations.

Finally, we briefly discuss the basal slip KBC and the flow dynamics within the basal shear band, which could not be captured by any of the aforementioned models. Different from fluids, a basal slip KBC is common in granular currents on smooth basal surfaces (e.g. Savage and Hutter 1991; GDR MiDi 2004; Sheng et al. 2011), though a quantitative description of the slip velocity as a function of the flow quantities is still a challenging open problem (Artoni and Richard 2015). To our knowledge, the few works that tried to quantitatively study the slip KBC in the dense regime are the numerical investigations by Artoni et al. (2009, 2012, 2015), in which a strictly increasing relationship between the effective wall friction coefficient, $\mu_{\text{eff}} = (\tau_{xz}/\sigma_z)|_{z=0}$, and a suitable dimensionless slip velocity is found.

In our experimental investigation, the basal slip velocity is inaccessible by the PIV technique, which is based on spatial averaging. However, by comparing the PIV measurements near the bed (cf. Fig. 6a) with a naked-eye particle tracking analysis, we found that the PIV measurements at $z = d/2$, $u_x|_{z=d/2}$, can be regarded as reliable estimations of the translational velocity of the lowest layer of grains. As mentioned in Sect. 2.2, from naked-eye observation it also emerged that only a weak basal grain rolling occurs on the surface S . Hence, $u_x|_{z=d/2}$ has been taken as a rough estimation of the slip velocity. A diagram of $u_x|_{z=d/2}$ as function of z_f is reported in Fig. 7, where it is evident $u_x|_{z=d/2}$ that noticeably decreases as z_f increases.

This trend is mainly due to the resistances exerted at the sidewalls. To explain this, consider that the basal shear stress, τ_{xz} , required for balancing the x -component momentum of a column of granular material, decreases with the flow depth, owing to the sidewall resistances, which in turn increase it (cf. “Appendix”). As the basal normal stress, σ_z , increases with z_f , it follows that the effective friction at the basal surface $\mu_{\text{eff}} = (\tau_{xz}/\sigma_z)|_{z=0}$ decreases with it. Now, by reasonably assuming that the slip velocity increases with μ_{eff} , in accordance with that observed numerically by Artoni et al. (2009, 2012, 2015), it follows that increasing flow depths imply decreasing basal slip velocities, which is what we found experimentally. Another concurrent cause of the decrease of $u_x|_{z=d/2}$ is probably the confining effect of the basal normal stress, σ_z ,

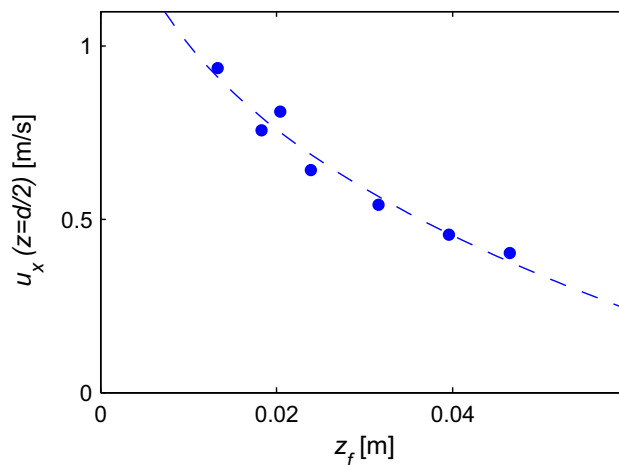


Fig. 7 Experimental relationship between the slip velocity, $u_x|_{z=d/2}$, and the flow depth, z_f , on surface S . Best-fitting curve: $u_x|_{z=d/2} = 1.98 - 4.32 z_f^{0.32}$

which increases with the flow depth (cf. “Appendix”). In fact, the grain dilatancy, required for the basal shear to develop, is progressively inhibited by increasing values of σ_z .

Assuming for sake of simplicity that the initial velocity at the inflow cross section ($x = 0$ m) is null, the velocity $u_x|_{z=d/2}$ at the cross section under study is certainly limited by the theoretical velocity of free fall on an inclined plane, $u_{x,ff} = \sqrt{2gx \sin \beta} = 1.98$ m/s, with $x = 0.4$ m and $\beta = 30^\circ$. Based on this simple assumption, we found that all $u_x|_{z=d/2}$ on S -type bed can be well described by the function, $u_x|_{z=d/2} = u_{x,ff} - a z_f^b = 1.98 - 4.32 z_f^{0.32}$ (cf. Fig. 7). It is difficult to find a clear physical explanation for the best-fitting value of the exponent ($b = 0.32$), since it does depend critically both on the unknown function accounting for the rate-dependent basal shear stress and also on the unknown sidewall friction, which is expected to show a rate dependency as well and a non-unitary earth-pressure coefficient (cf. “Appendix”).

3.2.2 Sidewall Measurements: Experiments on Surface G (Granular Bed)

We now proceed to present the sidewall measurements of experiments on surface G (Fig. 8). The roughness of surface G always guarantees a no-slip KBC. Moreover, the characteristic length of the roughness is large enough to prevent any grain rolling. Analogous to Exp-10G already shown in Sect. 3.1, from Fig. 8a, it is evident that all \bar{u}_x profiles exhibit an upper approximately linear part (*surface flow* layer, denoted by the symbol “2”) and a lower convex zone (*creep flow* layer, denoted by the symbol “1”). Similar to the runs on S -type bed, $\dot{\gamma}$ is found to decrease in

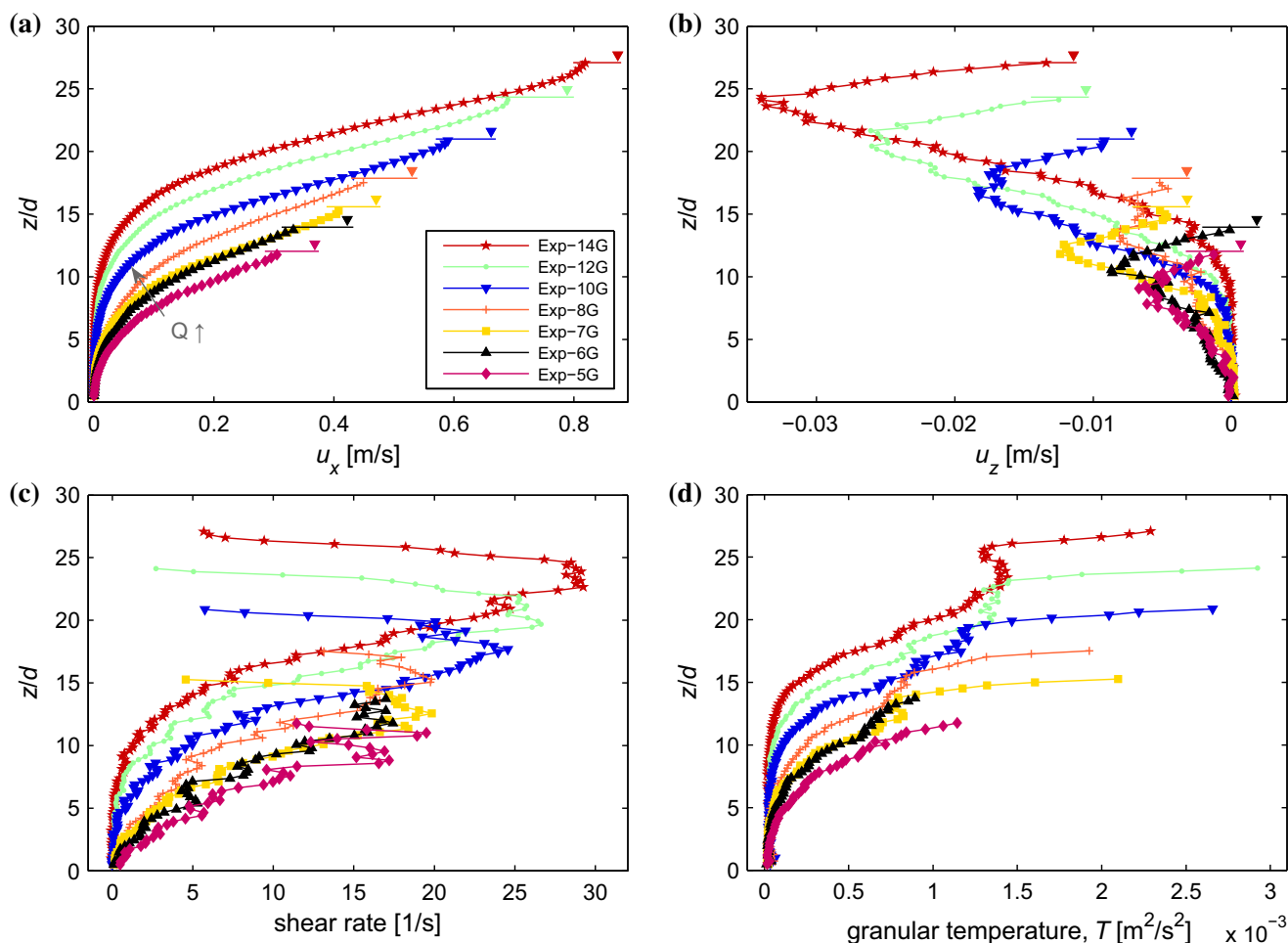


Fig. 8 Sidewall velocity profiles of experiments on surface *G* (averages on four repetitions), **a** *x*-component, **b** *z*-component, **c** shear rate, **d** granular temperature

a thin zone near the free surface (cf. Fig. 8c), though the trend is less clear in the experiments with small flow depths and, consequently, smaller flow velocities. In particular, a thin concavity of the velocity profiles appears close to the free surface (cf. Fig. 8a), in experiments Exp-10G, Exp-12G and Exp-14G, characterized by larger velocities at the free surface.

It is worth underlining that the observed \bar{u}_x profiles are in general agreement with other experimental works, obtained in different geometries, such as heap flows or rotating drum geometries (e.g. Komatsu et al. 2001; Bonamy et al. 2002; Jop et al. 2005). It suggests that the presence of a rigid bed weakly influences the flow pattern, if the thickness, h_1 , of the lower *creep flow* is large enough. Following Komatsu et al. (2001), the convex velocity profile in the *creep flow* layer can be described by an exponential function

$$\bar{u}_{x,1}(z) = u_0 \exp(1/\lambda(z - z_f)), \tag{9}$$

where u_0 is a parameter with dimension of a velocity and λ is a decay characteristic length. A physical explanation of such an exponential decay of velocities probably lies behind the concomitance of a number of effects: long-lasting frictional contacts, sidewall friction, non-local effects due to force chains and the slow processes of void creation in the creeping bulk, observed by Komatsu et al. (2001). Conversely, the flow in the upper layer, 2, of width $h_2 = z_f - h_1$, can be approximately described by the linear function

$$\bar{u}_{x,2}(z) = \bar{u}_x|_{z=h_1} + b_l(z - h_{creep}), \tag{10}$$

where $\bar{u}_x|_{z=h_1}$ is the flow velocity measured at the interface between the creep flow and the upper flow, and b_l is the average shear rate (obtained by best fitting) in the upper surface flow. Similar to the optimization algorithm proposed for the composite fits of *S*-type experiments, reported in Sect. 3.2.1, the best interface position was identified

here by simply choosing the composite best-fitting curve that exhibits the minimum jump of the velocity derivatives at the interface, $|\partial_z \bar{u}_{x,1} - \partial_z \bar{u}_{x,2}|$. The best-fitting parameters of both curves are reported in Table 5, together with the normalized depths of both the creep flow, h_1/d , and the surface flow, h_2/d .

As it is shown in Table 5, h_2 varies between $4.5d$ and $8d$ and increases with Q_m . As well, the characteristic length, λ , of the exponential decay weakly increases with Q_m and consequently with z_f : λ is always of order of the particle diameter d with values $2.2d \leq \lambda \leq 3.1d$ and is, hence, highly similar to the one observed by Bonamy et al. (2002), $\lambda = 2.5d$, in a rotating drum geometry. Compared to other experimental data, obtained in semi-infinite geometries (e.g. Komatsu et al. 2001), the weak increase of λ with z_f suggests that the rate of the velocity decay in the lower zone is not only a function of the granular material but it seems to depend also on the presence of the fixed rough basal surface, at least as long as the total flow depth is small. Conversely, it is reasonable to infer that for very high flow depths, and, consequently, in presence of a deep enough creep flow layer, λ should tend asymptotically to the same value obtainable in a semi-infinite geometry, not depending on the properties of the rough basal surface.

Similar to that observed on S -type basal surface, the \bar{u}_z velocity profiles exhibit a minimum at around $3d-5d$ from the free surface in all runs. We point out that this trend is clearly visible also in Exp-5G and Exp-6G, which correspond to almost uniform steady states and, consequently, exhibit approximately null values of \bar{u}_z at the free surface. This clearly confirms that such a secondary flow beneath the free surface occurs independently from the inclination of the free surface.

The $\dot{\gamma}$ profiles (Fig. 8c) exhibit an exponential behaviour in the lower creep flow, an approximately constant trend (though disturbed by some oscillations) in the upper surface flow and, finally, a thin decreasing zone close to the free surface, corresponding to the thin concavity, already observed in some \bar{u}_x profiles. It is worth noting that the averaged value of $\dot{\gamma}$ in the surface flow increases with the

mass flow rate, Q_m , (cf. parameter b_1 in Table 5). Its range of variation is comparable with data available in the literature (GDR MiDi 2004) and confirms that $\dot{\gamma}$ is also slightly influenced by the resistances of the sidewalls (Jop et al. 2005). Finally, the granular temperature profiles (Fig. 8d) show a lower tail, corresponding to the creep flow, where the values are typically smaller than $0.5 \times 10^{-3} \text{ m}^2/\text{s}^2$. Conversely, in the upper region, T is between $0.5 \times 10^{-3} \text{ m}^2/\text{s}^2$ and $3 \times 10^{-3} \text{ m}^2/\text{s}^2$. The joined information of \bar{u}_x and T profiles supports the occurrence of a rheological stratification, where a dense-collisional surface flow is superimposed on a prevalently frictional lower layer. To locate these two regions by using the granular temperature, a crude threshold of T could be found between $\approx 0.5 \times 10^{-3} \text{ m}^2/\text{s}^2$ and $\approx 1 \times 10^{-3} \text{ m}^2/\text{s}^2$. For comparison, note that in runs on surface S , where the flow dynamics is more prevalently collisional, T is not smaller than $10^{-3} \text{ m}^2/\text{s}^2$ all along the flow depth (cf. Sect. 3.2.1).

3.2.3 Sidewall Measurements: Experiments on Surface R (Sandpaper Bed)

The sidewall measurements, related to the experiments on surface R, are reported in Fig. 9. Analogous to the G -type surface, a no-slip bottom KBC occurs here. Yet, grain rolling at the basal surface is allowed thanks to the small characteristic length of the sandpaper roughness. As a result, non-null PIV velocities are observed at the bed and they are found to decrease with increasing values of z_f . The grain rolling at the bed is chiefly governed by the normal stress at the basal surface and by the frictional resistances at the sidewalls. We underline that these rolling phenomena are crucial for correctly understanding the various shapes of the flow velocities profiles on surface R. In fact, the \bar{u}_x profiles exhibit very different behaviours, depending on the flow depth and on the grain velocity at the bed (Fig. 9a). To this regard, the experimental results could be grouped into three families: the first family only contains Exp-5R, characterized by the lowest flow depth; the second family contains the runs with high flow depths (Exp-8R,

Table 5 Best-fitting parameters of the exponential (9) and linear (10) models for the \bar{u}_x velocity profiles on G surface, together with the normalized depths of both layers, h_1/d and h_2/d

Run	Lower exponential model			Upper linear model			h_1/d	h_2/d
	u_0 (ms ⁻¹)	λ (mm)	R^2	$\bar{u}_x _{z=h_1}$ (ms ⁻¹)	b_1 (s ⁻¹)	R^2		
Exp-5G	0.890	7.17	0.983	0.10	14.05	0.991	7.27	4.55
Exp-6G	0.841	8.23	0.986	0.11	13.93	0.990	9.09	4.85
Exp-7G	1.202	8.35	0.991	0.14	16.95	0.998	10.30	5.15
Exp-8G	0.959	10.61	0.989	0.15	16.46	0.996	12.12	5.76
Exp-10G	1.574	9.88	0.995	0.19	20.87	0.997	14.85	6.36
Exp-12G	2.358	9.98	0.997	0.20	22.10	0.994	16.97	7.27
Exp-14G	3.192	10.16	0.998	0.22	23.97	0.993	19.09	8.18

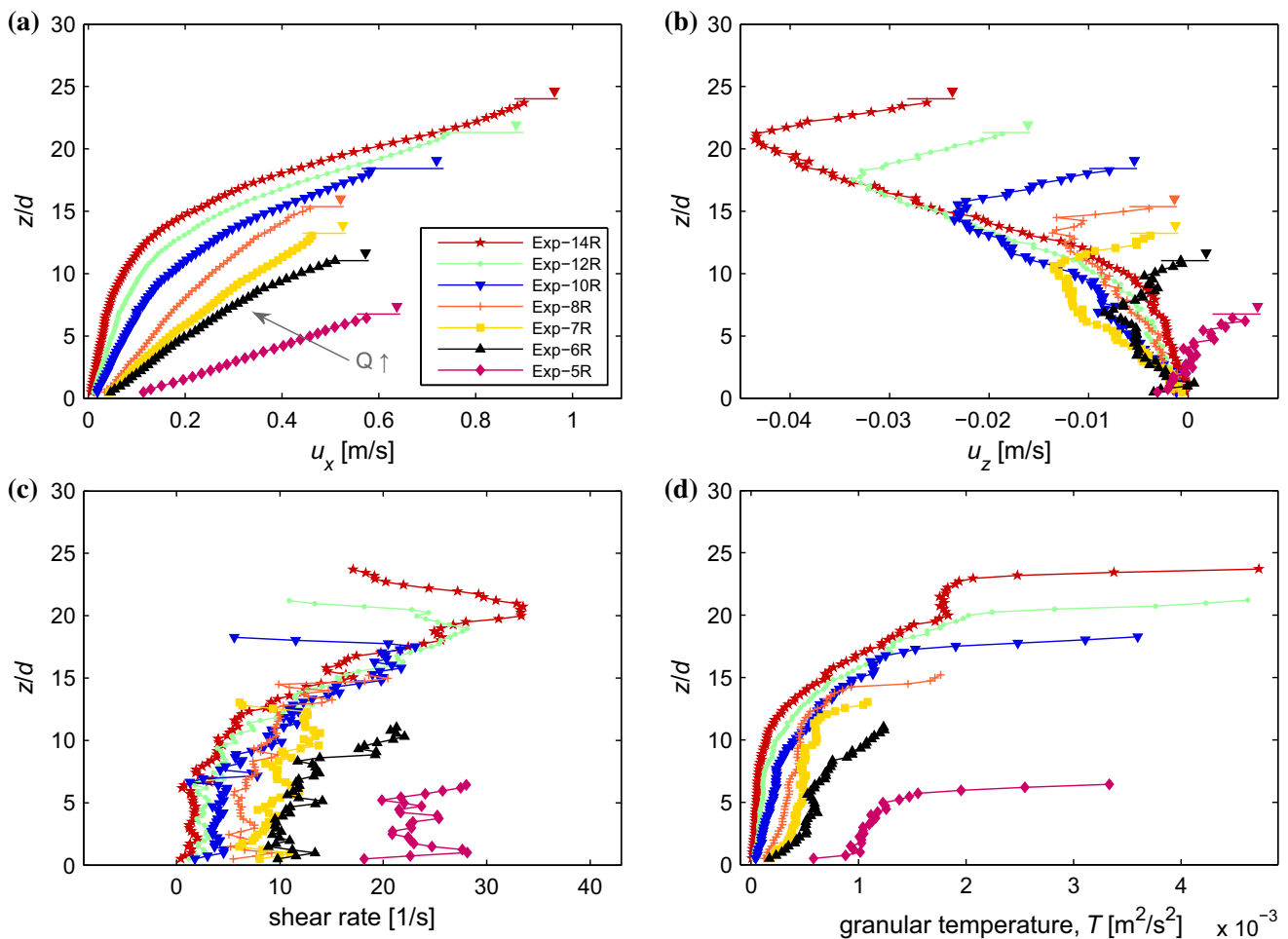


Fig. 9 Sidewall velocity profiles of experiments on rough sandpaper bottom surface (averages on four repetitions), **a** x -component, **b** z -component, **c** shear rate, **d** granular temperature

Exp-10R, Exp-12R and Exp-14R); and the third one contains the runs with intermediate flow depths (Exp-6R, Exp-7R).

In Exp-5R, where the flow depth is only $\approx 5d$, the velocity profile is rigorously linear with an averaged shear rate (obtained through best fitting) $\dot{\gamma} = 23.27 \text{ s}^{-1}$, highly similar to the velocity profiles observed on surface S . Conversely, in Exp-10R, Exp-12R and Exp-14R, corresponding to larger values of z_f , the velocity profiles clearly exhibit a lower exponential tail and an approximately linear upper zone, analogous to that observed on surface G . Therefore, for these runs, the same composite fit, already used to describe the velocity profiles on G -type bed, is employed. The best-fitting parameters of both the exponential (9) and linear (10) functions are reported in Table 6.

Also, Exp-8R can be partially considered as part of this group of experiments, and thus, it has been reported in Table 6. Yet, in this case, although the upper part of the velocity profile can be still well described by a linear

function, the lower velocity profile exhibits a weak convexity that cannot be properly described by an exponential function (cf. Fig. 9a–c). From Table 6, it is clear that h_1 weakly increases with Q_m , analogous to the runs on surface G . Differently, the characteristic length of decay, λ , is found to decrease with z_f and has noticeable larger values ($4.7d$ – $7.2d$) than those observed on surface G . It confirms that the decay length of the exponential tail is not only a function of the granular material but it also depends on the flow dynamics, which in turn is influenced by the rough basal surface. As expected, if the flow depth increases, the decay length becomes closer and closer to that observed on surface G , meaning that the influence of the rigid bed on λ progressively fades out, due to the formation of a deep enough creep flow nearby the rigid surface, which practically acts as a buffer layer separating the active flow from the fixed boundary.

In the third group of experiments (Exp-6R and Exp-7R), the \bar{u}_x profiles gradually deviate from the linear profile and start exhibiting a weak convexity in their lower zone. It is

Table 6 Best-fitting parameters of the exponential (9) and linear (10) models for the \bar{u}_x velocity profiles of Exp-8R, Exp-10R, Exp-12R and Exp-14R, together with the normalized depths of both layers, h_1/d and h_2/d

Run	Lower exponential model			Upper linear model			h_1/d	h_2/d
	u_0 (ms ⁻¹)	λ (mm)	R^2	$\bar{u}_x _{z=h_1}$ (ms ⁻¹)	b_1 (s ⁻¹)	R^2		
Exp-8R	0.530	23.66	0.981	0.33	12.95	0.992	12.42	2.73
Exp-10R	0.670	20.00	0.997	0.38	20.05	0.998	15.15	3.33
Exp-12R	0.907	17.81	0.999	0.38	24.49	0.997	16.67	4.85
Exp-14R	1.442	15.51	0.999	0.42	28.31	0.994	18.18	5.76

worth underlining that the lower convex part of these intermediate velocity profiles cannot be described at all by an exponential law of the kind of Eq. (9). These intermediate experiments clearly represent a transition regime between the linear scaling of Exp-5R and the stratified exponential-linear profiles, observed in experiments with higher flow depths. This experimental finding represents an important result of the present research, since, to our knowledge, it is the first time that a transition regime of this kind has been observed in a channelized geometry. The fact that the flow velocity profiles gradually shift from a linear to a convex shape evidently indicates that different dissipation mechanisms progressively enter to play, as the flow depth increases. Finally, it is worth noting that the sidewall velocity at the free surface decreases with the flow depth from Exp-5R to Exp-8R (cf. Fig. 9a), which might appear surprising as the flow rate Q_m increases. Differently, it starts to increase again from Exp-8R to Exp-14R. We believe that this unexpected behaviour derives from the fact that different flow regimes occur by varying the flow depth.

The z -component velocity profiles are very similar to those observed in experiments on G -type basal surface, with the minimum occurring $\approx 4d$ below the free surface. A partial exception of this trend is represented by Exp-5R, which is the only experiment showing $\partial_x z_f > 0$ at the cross section under study, and, consequently, exhibits $u_z > 0$ along a depth of $\approx 3d$ below the free surface and, $u_z \approx 0$ for greater depths. The T profiles of Exp-8R, Exp-10R, Exp-12R and Exp-14R exhibit a similar behaviour of that observed in experiments on surface G . Values of T , generally smaller than $\approx 1 \times 10^{-3} \text{ m}^2/\text{s}^2$, are observed in the lower part of the flow, corresponding to the exponential tail. Differently, in Exp-5R, the granular temperature is almost constant and equal to $\approx 1 \times 10^{-3} \text{ m}^2/\text{s}^2$, with the exception of a thin layer in the vicinity of the free surface. The shape of this diagram is very similar to the T profiles observed on surface S , apart from the lack of the relative maximum at the bed. As expected, an intermediate behaviour of the T profiles is observed for experiments Exp-6R and Exp-7R, where the lower creep flow is not yet fully developed.

The aforementioned findings of this investigation on surface R clearly show that the angle of friction between grains and the basal surface is not sufficient for dynamically characterizing the basal surface. In fact, the large differences among the velocity profiles on G -type and R -type beds reveal that also the characteristic length of the basal roughness plays a crucial role, as it strongly influences the flow dynamics through allowing grain rolling at the bed. On the other hand, it should be kept in mind that, as the thickness of the lower creep flow becomes large enough (e.g. Exp-14R), the influence of the characteristic length of the basal roughness becomes less and less important. In this case, the frictional lower layer represents a buffer layer for the more active surface flow, and thus, the only relevant aspect for determining the velocity profile is the occurrence of a no-slip KBC and the absence of grain rolling at the fixed bed.

3.2.4 Summary of the Different Kinds of Sidewall Velocity Profiles

A panel plot, summarizing all the observed shapes of sidewall velocity profiles, is reported in Fig. 10. For the sake of clarity, only a selection of the experimental data set is shown in the figure. The parameters of the best-fitting functions are those already reported in Tables 3, 4, 5 and 6. In summary:

- Independently from the roughness of the basal surface, the composite shapes of the \bar{u}_x profiles signal a rheological stratification, occurring if the flow depth is high enough.
- The velocity profiles on surface S can be well described by a fully Bagnold scaling only at small flow depths, z_f . At larger z_f , the profiles can be better described by recurring to a composite function, composed of a linear fit for the lower layer and a Bagnold fit for the upper one (Fig. 10a).
- On surface G , all the velocity profiles show an exponential tail and an approximately linear upper profile (Fig. 10b).
- The velocity profiles on surface R are strongly influenced by the kinematic condition at the basal surface.

In the presence of intense grain rolling at the bed, occurring with small enough flow depths (Exp-5R), the profile appears linear. As z_f increases, the velocity profiles gradually become more and more convex in their lower zone, and eventually, for large flow depths they exhibit a lower exponential tail, analogous to that observed on surface *G* (Fig. 10c).

3.2.5 Free-Surface Velocity Profiles

The ensemble-averaged velocity profiles, measured at the free surface, are reported in Fig. 11. In order to compare all the profiles together more easily, we chose to normalize $\bar{u}_x|_{z_f}$ by $\bar{u}_{x,max}|_{z_f}$ (Fig. 11a, c, e). Nonetheless, information about the magnitude of $\bar{u}_x|_{z_f}$ in different runs can be straightforwardly deduced from the sidewall PIV measurements (cf. Figs. 6a, 8a, 9a). Conversely, we chose to keep $\bar{u}_y|_{z_f}$ in dimensional form so as to give information of the related magnitudes (Fig. 11b, d, f).

All the x -component velocity profiles show a symmetric, approximately parabolic, shape with the maximum, $\bar{u}_{max}|_{z_f}$, at $y = W/2$ and minima at the side walls, which was expected due to wall friction. Differently, the y -component velocity profiles exhibit an anti-symmetric behaviour with approximately null values at $y = W/2$ and at the side walls. As regards the experiments on surface *S*, interestingly all the \bar{u}_x/\bar{u}_{max} plots approximately collapse into a unique profile (Fig. 11a). Differently, \bar{u}_y increase with the flow rate (Fig. 11b) and show maximum absolute values, $|\bar{u}_y|$, ranging between ≈ 0.005 m/s (Exp-5S) and ≈ 0.02 m/s (Exp-14S) and located at $y/W \approx 0.2$ and $y/W \approx 0.8$. For Exp-5S and Exp-6S, the anti-symmetric shape of \bar{u}_y is not clearly visible, due to the very small values of \bar{u}_y , which are comparable with the PIV accuracy. As regards the experiments on *G*- and *R*-type beds (Fig. 11c–e), the \bar{u}_x/\bar{u}_{max} profiles become blunter and blunter, as Q_m increases. This result reveals that the momentum exchange mechanisms at the free surface, due to mass exchanges across y -direction, tend to flatten the x -component velocity profile in a turbulent-like fashion. Though for slow flows the sidewall resistances can be approximately assumed to be purely frictional (e.g. Jop et al. 2005), in case of large flow velocities a rate-dependent resistance is also expected to develop at the side walls, and consequently, it is expected to make the shear rate grow along y -direction. The fact that this does not happen (the profiles become blunter) suggests that the collisional momentum exchanges along y -direction (deducible from \bar{u}_y profiles in Fig. 11) are dominant, as the flow velocities increase. Finally, the \bar{u}_y -profiles of runs on *G*-type and *R*-type beds are chiefly anti-symmetric and are found to approximately collapse onto unique plots

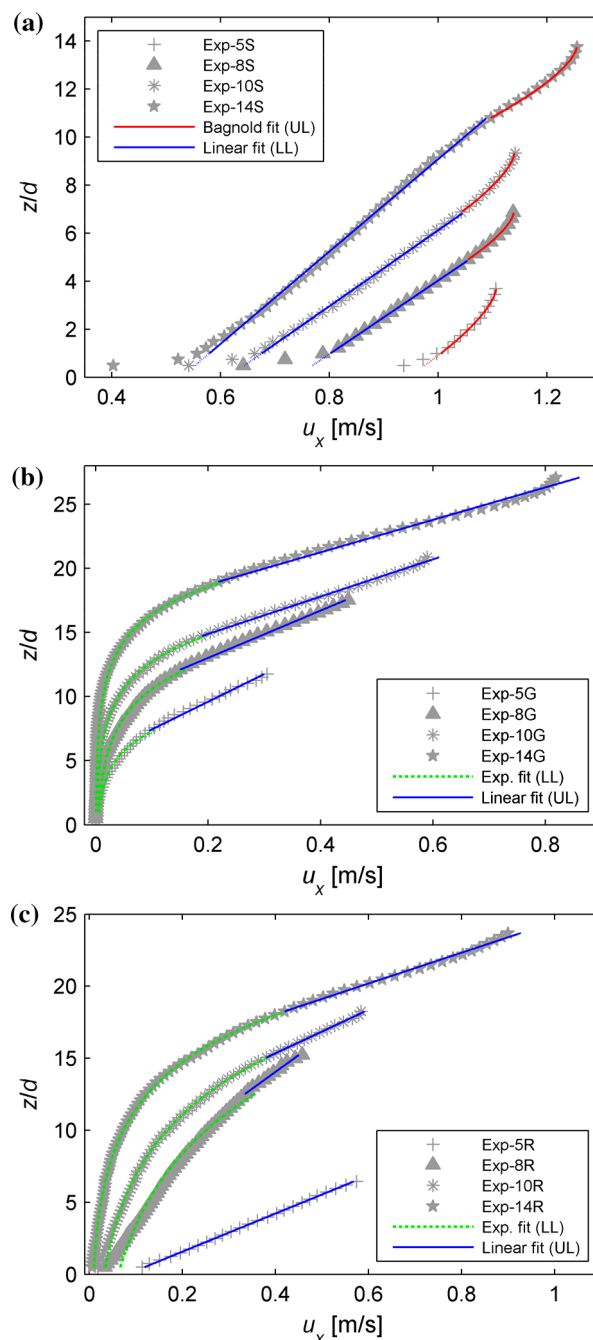


Fig. 10 Summary plot showing the different shapes of sidewall velocity profiles. **a** Surface *S*: Bagnold and linear fitting functions for the upper (UL) and lower layer (LL), respectively; **b** surface *G*: linear and exponential fitting functions for the upper (UL) and lower layer (LL), respectively; **c** surface *R*: linear and exponential fitting functions for the upper (UL) and lower layer (LL), respectively

(Fig. 11d–f), showing maxima expectedly smaller than the values observed on surface *S*. The only exception is represented by the \bar{u}_y profile of Exp-5R (in Fig. 11f), where the anti-symmetric shape is lost, probably due to PIV errors, which are of the same order of the measurements.

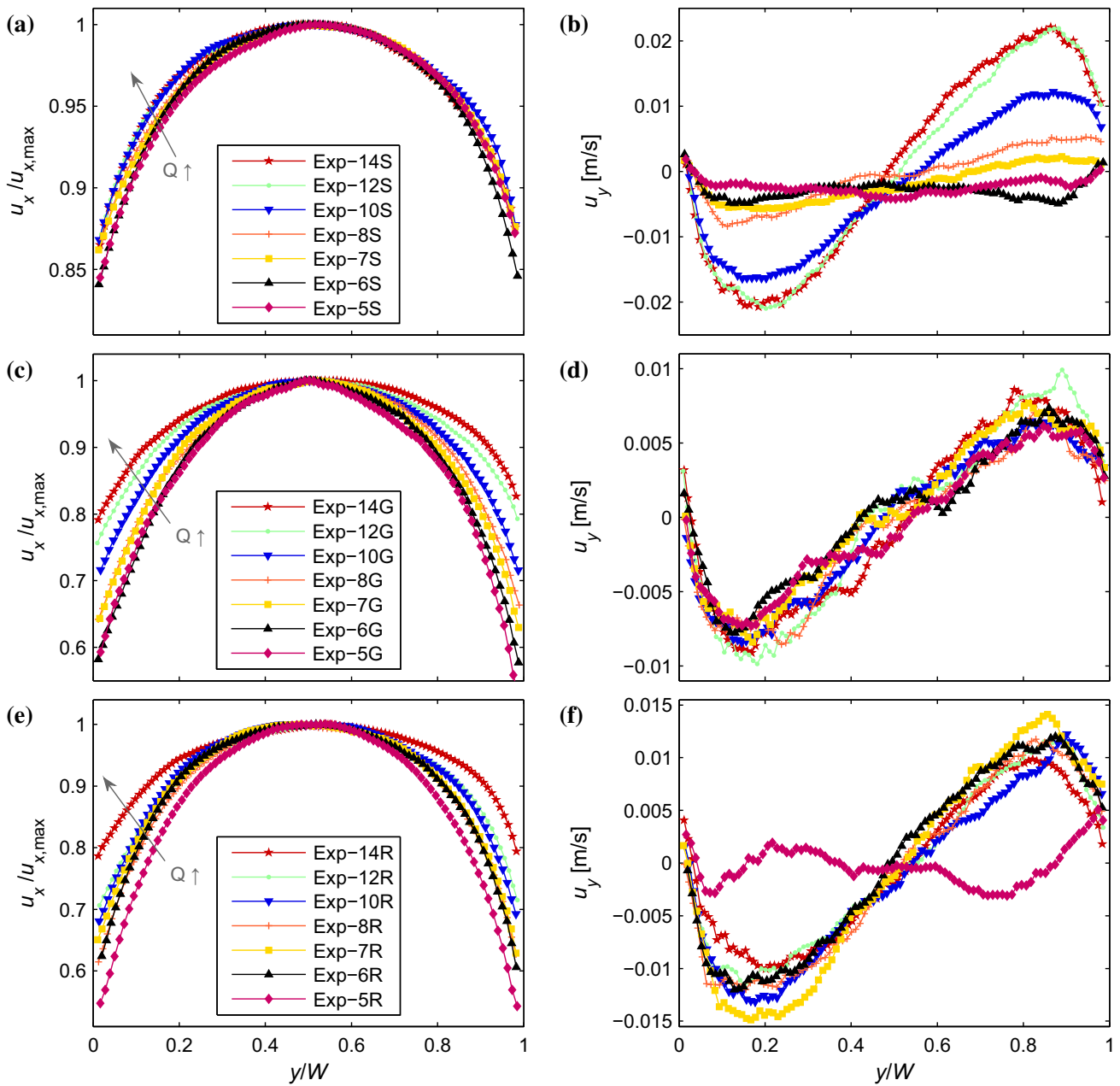


Fig. 11 Profiles of $\bar{u}_x/\bar{u}_{x,max}$ and \bar{u}_y at the free surface: **a, b** experiments on surface *S*, **c, d**, experiments on surface *G*, **e, f** experiments on surface *R*

A synthetic indicator of the shape of the $\bar{u}_x(y)$ profile at the free surface could be defined as the ratio between the *y*-averaged value of \bar{u}_x and its value at the side wall, $\bar{u}_x|_{y=0}$

$$\alpha_f = \frac{1}{W} \int_0^W \bar{u}_x(y) dy \cdot \frac{1}{\bar{u}_x|_{y=0}} \tag{11}$$

Obviously, given the shape of the velocity profiles (cf. Fig. 11), α_f is always greater than 1. The plots of α_f as a function of Q_m are reported in Fig. 12. For runs on surface *S*, α_f is practically constant and equal to ≈ 1.12 , which is

congruent with the curve collapse observed in Fig. 11a. Differently, the runs on the *R*- and *G*-type beds exhibit decreasing values of α_f with Q_m . For any given value of Q_m , different values of α_f are observed for different basal surfaces. By simply assuming that α_f should asymptotically tend to 1 as $Q_m \rightarrow \infty$, a good fitting of the relationship $\alpha_f - Q_m$ on *G*-type and *R*-type series can be obtained by using functions of the type: $\alpha_f = 1 + a Q_m^{-b}$. In addition, we plotted α_f as a function of the flow depth, z_f in Fig. 13. We interestingly found that data, obtained from runs on *G*- and *R*-type beds, collapse into a unique linear plot, meaning

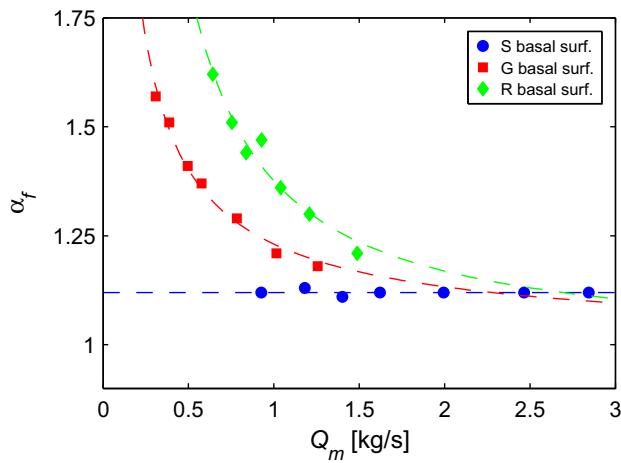


Fig. 12 Diagrams of α_f as function of Q_m at different basal surfaces. Fitting curves are $\alpha_f = 1.12$ for surface S , $\alpha_f = 1 + 0.23Q_m^{-0.80}$ for surface G , $\alpha_f = 1 + 0.38Q_m^{-1.15}$ for surface R

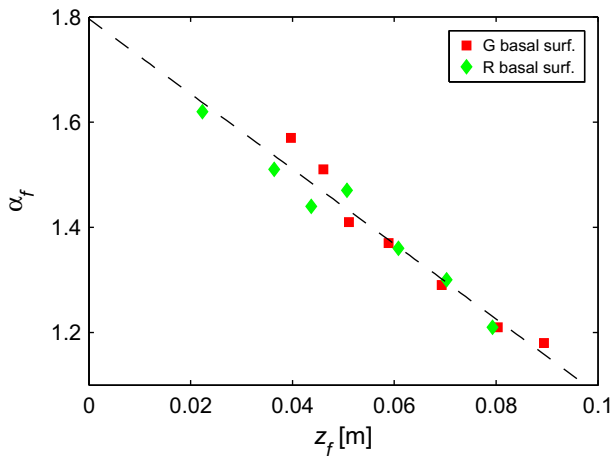


Fig. 13 Plots of α_f as function of z_f (G - and R -type beds). The best-fitting curve is $\alpha_f = 1.795 + 7.13 z_f$

that α_f only depends on z_f regardless of the different basal surfaces. It suggests that the effects of rough basal surfaces on the flow dynamics at the free surface are only mediated by z_f .

Since the channelized granular flows are clearly three dimensional, as apparent from the free-surface measurements, the flow velocities, measured from the sidewall, might differ from the velocity field inside the flow domain. However, it is typically impossible to get optical measurements inside a non-transparent dense granular medium. Following an approach similar to that proposed by Sheng et al. (2011), here we provide an approximate estimation of the width-wise averaged velocity profile, which exploits the PIV velocity measurements at the free surface. It is assumed that the flow velocity at any given z approximately scales as the flow velocity at the free surface, i.e.

$$\bar{u}_x(y, z) \approx \frac{\bar{u}_x(y, z_f)}{\bar{u}_x(0, z_f)} \bar{u}_x(0, z) \quad \forall z, \tag{12}$$

where $\bar{u}_x(0, z)$ represents the PIV measurement at the sidewall and $\bar{u}_x(y, z_f)$ is the PIV measurement at the free surface at the coordinate y . Under assumption (12), the width-wise averaged velocity profile, $\bar{u}_{x,y\text{-averaged}}$, can be estimated by multiplying the sidewall velocity profile, $\bar{u}_x(0, z)$, by the factor α_f previously defined in (11): $\bar{u}_{x,y\text{-averaged}}(z) = \frac{1}{W} \int_0^W \bar{u}_x(y, z) dy \approx \alpha_f \bar{u}_x(0, z)$. In the case of relatively small flow depths and basal slip KBC, this estimation appears reasonable, as the velocity variations inside the cross section are limited in a narrow range. Clearly, assumption (12) might become less precise in cases of no-slip KBC or high flow depths (e.g. Ahn et al. 1991; Sheng et al. 2011).

4 Conclusions

In this paper, an experimental investigation on steady channelized dry granular flows is presented, with particular attention being given to the effects of the rigid boundaries. Using a fixed inclination of 30° , a data set of 21 experiments (each repeated four times) was obtained by systematically varying the upstream boundary conditions and by employing three kinds of basal surfaces with different roughness. The laboratory apparatus was equipped with two high-speed cameras and a flickering-free LED light, which, in conjunction with the open-source PIV code PIVlab, represents an efficient and cost-effective set-up for getting velocity measurements in granular flows. Thanks to its multi-pass capabilities, the code PIVlab allowed to obtain reliable measurements, even in the presence of high shear rates.

Very different shapes of the sidewall velocity profiles were observed by varying both the basal surface and the flow depth. A distinct influence of the flow depth on the velocity profiles was discovered even in the presence of the same basal surface. In particular, it has been found that the sidewall resistances and the confining pressures are capable of enforcing a rheological stratification on all investigated basal surfaces, provided that the flow depth becomes high enough. To this regard, various composite functions, formed of the Bagnold, linear and exponential scalings, have been proposed to correctly describe the sidewall x -component velocity profiles.

In runs on the smooth basal surface (S), a shear band was systematically observed at the bed, where the slip velocities could be well described by a simple power law function of the flow depth. In case of small flow depths, the sidewall velocity profiles could be well described by a

Bagnold scaling. For larger flow depths, the Bagnold scaling alone becomes inadequate. Differently, the velocity profiles could be better described by recurring to a composite fit, made up of a linear model for the lower layer and a Bagnold scaling for the upper one. The gradual shift from a Bagnold to a composite linear scaling could be explained by the combined effects of sidewall resistances and of force chains, causing non-local dissipation mechanisms (Mills et al. 1999). While the dissipation mechanisms may be still prevalently collisional, as supported by the diagrams of the granular temperatures, the Bagnold scaling is progressively obscured by these effects with the increase in the flow depth. The complex interplay between the granular dynamics and fixed boundaries, especially in the proximity of the bed and of the free surface, is worth further experimental investigations, where additional measurements of the near-wall volume fraction and of the shear stresses could represent crucial improvements.

As regards the experiments on the roughened basal surface G , enforcing a no-slip KBC, stratified frictional-collisional flows, with an exponential lower tail and an upper approximately linear velocity profile, were observed in all runs. This is in agreement with other experimental works, obtained in semi-infinite geometries (Komatsu et al. 2001), and suggests that the roughness of the fixed bed becomes irrelevant, if a deep enough creep flow, acting as a buffer layer for the upper more active current, develops.

In the case of the sandpaper basal surface R , a no-slip KBC occurs but basal grain rolling is made possible by the small characteristic length of the roughness. At small flow depths, the velocity profile showed a non-null velocity at the bed, due to rolling, and a linear scaling, highly similar to the velocity profiles on the smooth surface. At higher flow depths, the basal rolling was progressively inhibited by the effects of the sidewall resistances and by the increasing confining pressure. As well, the velocity profiles were found to become more and more convex in their lower zones and, consequently, were observed to gradually shift to a stratified exponential-linear shape, similar to that observed on the rough surface G . The experimental discovery of the aforementioned transition regime on R -type bed, which can be regarded as a major result of the present research, on the one hand, underlines the great influence of the basal grain rolling and, in general, of the roughness of the bed surface, which is not simply characterized by an angle of friction but also by a characteristic length. On the other hand, it confirms that the peculiar roughness of the basal surface becomes unimportant if a sufficiently deep creeping lower layer develops.

Furthermore, in most of the investigated experiments, the z -component sidewall velocity profiles were found to be negative along the flow depth and showed a minimum at $\approx 4d$ below the free surface, regardless of the type of basal

boundary. This interesting finding, joined with the observation of the y -component velocities profiles at the free surface, strongly suggests the occurrence of a weak secondary circulating flow inside the cross section, probably allowed by relatively low values of the solid volume fraction beneath the free surface. Such a phenomenon merits further experimental investigations, possible with additional measurements of the near-wall volume fraction on which we are working.

The x -component velocity profiles at free surface showed a symmetric shape with minima at the sidewalls, confirming the non-negligible resistances there and the three-dimensional character of the channelized granular flows. An approximate estimation of the width-wise averaged velocity profiles, consisting of scaling the sidewall velocity profiles through using the velocity measurements taken from the free surface, has been proposed. Finally, the free-surface velocity profiles were found to gradually flatten with the increase in the mass exchanges along the y -direction, caused in turn by grain collisions.

The results of this experimental investigation, reporting a systematic comparison of velocity measurements over a wide range of flow depths and basal kinematic conditions, can be employed as a reference database for future modelling attempts.

Acknowledgements The authors wish to thank Ing. Nicola Immediata for his assistance in designing the experiments, Ing. Vito Foresta and Prof. Settimio Ferlisi (Laboratory of Geotechnical Engineering, Salerno Univ.) for the support in carrying out the shear tests on the granular material. The authors are also grateful to Ing. M. Palumbo, Ing. A. D'Amico and Ing. J. Tessitore for help in the experimental activity, given during the traineeship in their undergraduate programs at the Salerno University.

Compliance with Ethical Standards

Conflict of interest The authors declare that the research was conducted in the absence of any commercial or financial conflict of interest.

Appendix: Dissipation Mechanisms and Resistances at the Side Walls in Channelized Dry Granular Flows

The dissipation mechanisms in dense-collisional granular flows are essentially due to friction (long-lasting contacts among grains) and collisions (short-lasting contacts). Neglecting non-local effects (e.g. Mills and al. 1999) here for sake of simplicity, the deviatoric part of the stress tensor, Σ , may be written as the following generic function

$$\Sigma(x, y, z, t) = \Sigma\left(\overline{D}(x, y, z, t), P(x, y, z, t), c(x, y, z, t)\right), \quad (13)$$

where \overline{D} is the strain-rate tensor, P is the spherical part of the stress tensor and c is the solid volume fraction. Obviously, the function Σ also depends on the mechanical properties of the granular material, such as the internal friction angle, φ , and the coefficient of restitution, e . The dependency on P is determined by frictional mechanisms, while the dependency on \overline{D} is due to collisional momentum exchanges. For a two-dimensional flow in the xz plane, the shear stress τ_{xz} can be written as

$$\tau_{xz}(x, y, z, t) = \tau_{xz}(\dot{\gamma}(x, y, z, t), \sigma(x, y, z, t), c(x, y, z, t)), \quad (14)$$

where $\dot{\gamma}$ is the two-dimensional shear rate and σ is the spherical stress, $\sigma = (\sigma_x + \sigma_z)/2$. In the case of a uniform flow along the x -direction in an infinitely large channel and under the hypothesis that c is constant along the flow depth h , the force balance, projected along x , of a slice parallel to the free surface with thickness $h - z$ yields

$$\tau_{xz}(z) = \rho_s c g (h - z) \sin \beta, \quad (15)$$

where ρ_s is the grain density, g is the gravity acceleration and β is the inclination of the free surface with respect to the horizontal. As well, the z -component force balance equation yields

$$\sigma_z(z) = \rho_s c g (h - z) \cos \beta. \quad (16)$$

If the channel has a finite width, W , and the sidewalls are not perfectly smooth, the resistances exerted at the sidewalls should be considered in the force balance. Following the same approach by Jop et al. (2005), such additional resistances could be modelled through a purely Coulomb friction law (rate-dependent resistances are neglected here for the sake of simplicity). Assuming also that the flow can be still regarded as prevalently two dimensional (i.e. that the change of all physical quantities along y -direction is small), Eq. (15) can be rewritten as

$$\tau_{xz}(z) = \rho_s c g (h - z) \sin \beta - \frac{k_y \tan \varphi_{\text{wall}} \rho_s c g \cos \beta (h - z)^2}{W} \text{sgn}(u_x), \quad (17)$$

where φ_{wall} is the particle-wall angle of friction, W is the width of the flume, u_x is the x -component of the flow velocity, and k_y is a earth-pressure coefficient such that $\sigma_y = k_y \sigma_x$, assumed to be constant along the flow depth and meant to take into account the anisotropy of normal stresses (e.g. Savage and Hutter 1991). Equation (17) can be viewed as a generalization of that derived by Jop et al. (2005) and obtained by assuming the specific $\mu(I)$ rheology. Since the second term in the right-hand side of (17) is a quadratic function of $h - z$, at large values of $h - z$ it becomes dominant with respect to the other term, which is linear and accounts for the gravity force. Namely, $\tau_{xz}(z)$ is

expected to decrease with $h - z$ for big enough values of $h - z$ and eventually goes to 0. Even without considering any particular constitutive law for τ_{xz} , it is reasonable to assume that τ_{xz} is a strictly increasing function of $\dot{\gamma}$, owing to shear-dependent dissipation mechanisms (e.g. Savage 1984). As a consequence, $\dot{\gamma}$ is also expected to decrease with $h - z$, for big enough values of $h - z$. This prediction is qualitatively in good agreement with all the experimental data, reported in this work and with other data available in the literature (e.g. Bonamy et al. 2002; Taberlet et al. 2003; GDR MiDi 2004; Jop et al. 2005). It is worth noting that, even without the strong assumptions that c , k_y and φ_{wall} are constant along the flow depth, the aforementioned observations are still valid as long as c , k_y and φ_{wall} are bounded functions.

References

- Ahn H, Brennen CE, Sabersky RH (1991) Measurements of velocity, velocity fluctuation, density, and stresses in chute flows of granular materials. *J Appl Mech* 58(3):792–803
- Ancey C (2001) Dry granular flows down an inclined channel: experimental investigations on the frictional–collisional regime. *Phys Rev E* 65(1):1–19
- Ancey C, Evesque P (2000) Frictional–collisional regime for granular suspension flows down an inclined channel. *Phys Rev E* 62(6):8349
- Ancey C, Coussot P, Evesque P (1999) A theoretical framework for very concentrated granular suspensions in a steady simple shear flow. *J Rheol* 43:1673–1699
- Armanini A, Capart H, Fraccarollo L, Larcher M (2005) Rheological stratification in experimental free-surface flows of granular-liquid mixtures. *J Fluid Mech* 532:269–319
- Armanini A, Fraccarollo L, Larcher M (2008) Liquid–granular channel flow dynamics. *Powder Technol* 182(2):218–227
- Armanini A, Larcher M, Fraccarollo L (2009) Intermittency of rheological regimes in uniform liquid–granular flows. *Phys Rev E* 79:051306
- Artoni R, Richard P (2015) Effective wall friction in wall-bounded 3D dense granular flows. *Phys Rev Lett* 115(15):158001
- Artoni R, Santomaso A, Canu P (2009) Effective boundary conditions for dense granular flows. *Phys Rev E* 79(3):031304
- Artoni R, Santomaso AC, Go M, Canu P (2012) Scaling laws for the slip velocity in dense granular flows. *Phys Rev Lett* 108(23):238002
- Bagnold RA (1954) Experiments on a gravity-free dispersion of large solid spheres in a Newtonian fluid under Shear. *Philos Trans R Soc A Math Phys* 225(1160):49–63
- Baker JL, Barker T, Gray JMNT (2016) A two-dimensional depth-averaged $\mu(I)$ -rheology for dense granular avalanches. *J Fluid Mech* 787:367–395
- Bonamy D, Daviaud F, Laurent L (2002) Experimental study of granular surface flows via a fast camera: a continuous description. *Phys Fluids* 14(5):1666
- Capart H, Young DL, Zech Y (2002) Voronoï imaging methods for the measurement of granular flows. *Exp Fluids* 32(1):121–135
- da Cruz F, Emam S, Prochnow M, Roux J-N, Chevoir F (2005) Rheophysics of dense granular materials: discrete simulation of plane shear flows. *Phys Rev E* 72(2):021309

- Delannay R, Valance A, Mangeney A, Roche O, Richard P (2017) Granular and particle-laden flows: from laboratory experiments to field observations. *J Phys D Appl Phys* 50(5):053001
- Doyle EE, Hogg AJ, Mader HM (2010) A two-layer approach to modelling the transformation of dilute pyroclastic currents into dense pyroclastic flows. *Philos R Soc A Math Phys* 467:1348–1371
- Drake TG (1990) Structural features in granular flows. *J Geophys Res* 95(B6):8681–8696
- Eckart W, Gray JMNT, Hutter K (2003) Particle image velocimetry (PIV) for granular avalanches on inclined planes. In: Hutter K, Kirchner N (eds) *Dynamic response of granular and porous materials under large catastrophic deformations. Lecture notes in applied and computational mechanics*, vol 11. Springer, New York, pp 195–218
- Forterre Y, Pouliquen O (2008) Flows of dense granular media. *Ann Rev Fluid Mech* 40(1):1–24
- GDR MiDi (2004) On dense granular flows. *Eur Phys J E* 14(4):341–365
- Goodman MA, Cowin SC (1972) A continuum theory for granular materials. *Arch Ration Mech Anal* 44(4):249–266
- Jenkins JT, Savage SB (1983) A theory for the rapid flow of identical, smooth, nearly elastic particles. *J Fluid Mech* 130:187–202
- Jesuthasan N, Baliga BR, Savage SB (2006) Use of particle tracking velocimetry for measurements of granular flows: review and application. *Kona* 24:15–26
- Jiang Y-J, Towhata I (2013) Experimental study of dry granular flow and impact behavior against a rigid retaining wall. *Rock Mech Rock Eng* 46(4):713–729
- Jop P (2015) Rheological properties of dense granular flows. *Comptes Rendus Phys* 16(1):62–72
- Jop P, Forterre Y, Pouliquen O (2005) Crucial role of sidewalls in granular surface flows: consequences for the rheology. *J Fluid Mech* 541:167–192
- Jop P, Forterre Y, Pouliquen O (2006) A constitutive law for dense granular flows. *Nature* 441(7094):727–730
- Kamrin K, Henann DL (2015) Nonlocal modeling of granular flows down inclines. *Soft Matter* 11(1):179–185
- Kamrin K, Koval G (2012) Nonlocal Constitutive Relation for Steady Granular Flow. *Phys Rev Lett* 108(178301):1–5
- Komatsu T, Inagaki S, Nakagawa N, Nasuno S (2001) Creep motion in a granular pile exhibiting steady surface flow. *Phys Rev Lett* 86(9):1757–1760
- Lueptow RM, Akonur A, Shinbrot T (2000) PIV for granular flows. *Exp Fluids* 28(2):183–186
- Lun CKK, Savage SB, Jeffrey DJ, Chepurin N (1984) Kinetic theories for granular flow: inelastic particles in Couette flow and slightly inelastic particles in a general flowfield. *J Fluid Mech* 140:223–256
- Martino R, Papa MN (2008) Variable-concentration and boundary effects on debris flow discharge predictions. *J Hydraul Eng* 134(9):1294–1301
- Medina V, Hürlimann M, Bateman A (2008) Application of FLATModel, a 2D finite volume code, to debris flows in the northeastern part of the Iberian Peninsula. *Landslides* 5(1):127–142
- Mills P, Loggia D, Tixier M (1999) Model for a stationary dense granular flow along an inclined wall. *Europhys Lett* 45(6):733
- Nedderman RM, Tüzün U, Savage SB, Houlby GT (1982) The flow of granular materials. I. *Chem Eng Sci* 37(11):1597–1609
- Pirulli M, Mangeney A (2008) Results of back-analysis of the propagation of rock avalanches as a function of the assumed rheology. *Rock Mech Rock Eng* 41(1):59–84
- Pouliquen O (1999) Scaling laws in granular flows down rough inclined planes. *Phys Fluids* 11(3):542–548
- Pouliquen O, Forterre Y (2009) A non-local rheology for dense granular flows. *Philos Trans A Math Phys Eng Sci* 367(1909):5091–5107
- Prochnow M, Chevoir F, Mills P, Jenkins JT (2000) *Physique et Mécanique des Matériaux Granulaires*. Presses du LCPC, Champ-sur-Marne, p 425
- Pudasaini SP, Hsiau S-S, Wang Y, Hutter K (2005) Velocity measurements in dry granular avalanches using particle image velocimetry technique and comparison with theoretical predictions. *Phys Fluids* 17(9):093301
- Pudasaini SP, Hutter K, Hsiau S-S, Tai S-C, Wang Y, Katzenbach R (2007) Rapid flow of dry granular materials down inclined chutes impinging on rigid walls. *Phys Fluids* 19(5):053302
- Radjai F, Jean M, Moreau JJ, Roux S (1996) Force distributions in dense two-dimensional granular systems. *Phys Rev Lett* 77(2):274
- Sanchez T, Chen DTN, DeCamp SJ, Heymann M, Dogic Z (2012) Spontaneous motion in hierarchically assembled active matter. *Nature* 491(7424):431–434
- Sarno L (2013) *Depth-averaged models for dry granular flows*. Ph.D. thesis (University of Napoli Federico II)
- Sarno L, Martino R, Papa MN (2011a) Discussion of “Uniform flow of modified bingham fluids in narrow cross sections” by Alessandro Cantelli. *J Hydraul Eng* 137(5):621
- Sarno L, Papa MN, Martino R (2011). Dam-break flows of dry granular material on gentle slopes. In: Genevois R, Hamilton DL, Prestininzi A (eds) *Proceedings of the 5th international conference on debris-flow hazards mitigation: mechanics, prediction and assessment*, pp 503–512
- Sarno L, Carravetta A, Martino R, Tai Y-C (2013) Pressure coefficient in dam-break flows of dry granular matter. *J Hydraul Eng* 139(11):1126–1133
- Sarno L, Carravetta A, Martino R, Tai Y-C (2014) A two-layer depth-averaged approach to describe the regime stratification in collapses of dry granular columns. *Phys Fluids* 26(10):103303
- Sarno L, Papa MN, Villani P, Tai Y-C (2016) An optical method for measuring the near-wall volume fraction in granular dispersions. *Granul Matter* 18(4):80
- Sarno L, Carravetta A, Martino R, Papa MN, Tai Y-C (2017) Some considerations on numerical schemes for treating hyperbolicity issues in two-layer models. *Adv Water Resour* 100:183–198
- Savage SB (1979) Gravity flow of cohesionless granular materials in chutes and channels. *J Fluid Mech* 92:53–96
- Savage SB (1984) The mechanics of rapid granular flows. *Adv Appl Mech* 24:289–366
- Savage SB (1998) Analyses of slow high-concentration flows of granular materials. *J Fluid Mech* 377:1–26
- Savage SB, Hutter K (1991) The dynamics of avalanches of granular materials from initiation to runout. Part I: analysis. *Acta Mech* 86(1–4):201–223
- Scarano F, Riethmüller ML (2000) Advances in iterative multigrad PIV image processing. *Exp Fluids* 29(1):S051–S060
- Sheng L-T, Kuo C-Y, Tai Y-C, Hsiau S-S (2011) Indirect measurements of streamwise solid fraction variations of granular flows accelerating down a smooth rectangular chute. *Exp Fluids* 51(5):1329–1342
- Shojaee Z, Roux JN, Chevoir F, Wolf DE (2012) Shear flow of dense granular materials near smooth walls. I. Shear localization and constitutive laws in the boundary region. *Phys Rev E* 86(1):011301
- Silbert LE, Landry JW, Grest GS (2003) Granular flow down a rough inclined plane: transition between thin and thick piles. *Phys Fluids* 15(1):1–10
- Taberlet N, Richard P, Valance A, Losert W, Pasini JM, Jenkins JT, Delannay R (2003) Superstable granular heap in a thin channel. *Phys Rev Lett* 91(26):264301

- Taberlet N, Richard P, Henry E, Delannay R (2004) The growth of a super stable heap: an experimental and numerical study. *Europhys Lett* 68(4):515
- Thielicke W, Stamhuis E (2014) PIVlab—towards user-friendly, affordable and accurate digital particle image velocimetry in MATLAB. *J Open Res Softw* 2(1):e30. doi:[10.5334/jors.bl](https://doi.org/10.5334/jors.bl)
- Tubino M, Lanzoni S (1993) Rheology of debris flows: experimental observations and modelling problems. *Excerpta* 7:201–235
- Willert CE, Gharib M (1991) Digital particle image velocimetry. *Exp Fluids* 10(4):181–193